



UNIVERSITY OF LEEDS

This is a repository copy of *An integrated approach to determine three-dimensional accretion geometries of tidal point bars: Examples from the Venice Lagoon*.

White Rose Research Online URL for this paper:  
<https://eprints.whiterose.ac.uk/164219/>

Version: Accepted Version

---

**Article:**

Cosma, M, Yan, N [orcid.org/0000-0003-1790-5861](https://orcid.org/0000-0003-1790-5861), Colombera, L [orcid.org/0000-0001-9116-1800](https://orcid.org/0000-0001-9116-1800) et al. (3 more authors) (2020) An integrated approach to determine three-dimensional accretion geometries of tidal point bars: Examples from the Venice Lagoon. *Sedimentology*. ISSN 0037-0746

<https://doi.org/10.1111/sed.12787>

---

© This article is protected by copyright. All rights reserved. This is the peer reviewed version of the following article: Cosma, M, Yan, N , Colombera, L et al. (3 more authors) (2020) An integrated approach to determine three-dimensional accretion geometries of tidal point bars: Examples from the Venice Lagoon. *Sedimentology*. ISSN 0037-0746, which has been published in final form at <https://doi.org/10.1111/sed.12787>. This article may be used for non-commercial purposes in accordance with Wiley Terms and Conditions for Use of Self-Archived Versions. Uploaded in accordance with the publisher's self-archiving policy.

**Reuse**

Items deposited in White Rose Research Online are protected by copyright, with all rights reserved unless indicated otherwise. They may be downloaded and/or printed for private study, or other acts as permitted by national copyright laws. The publisher or other rights holders may allow further reproduction and re-use of the full text version. This is indicated by the licence information on the White Rose Research Online record for the item.

**Takedown**

If you consider content in White Rose Research Online to be in breach of UK law, please notify us by emailing [eprints@whiterose.ac.uk](mailto:eprints@whiterose.ac.uk) including the URL of the record and the reason for the withdrawal request.



[eprints@whiterose.ac.uk](mailto:eprints@whiterose.ac.uk)  
<https://eprints.whiterose.ac.uk/>

## **An integrated approach to determine three-dimensional accretion geometries of tidal point bars: Examples from the Venice Lagoon**

Cosma, Marta<sup>1,\*</sup>, Yan, Na <sup>2</sup>, Colombera, Luca <sup>2</sup>, Mountney, Nigel P.<sup>2</sup>, D'Alpaos, Andrea<sup>1</sup>, Ghinassi, Massimiliano<sup>1</sup>

<sup>1</sup> Department of Geosciences, University of Padova, Via Gradenigo 6, 35121 Padova, Italy

<sup>2</sup> Fluvial & Eolian Research Group, School of Earth & Environment, University of Leeds, LS2 9JT Leeds, UK

\* Corresponding author: [marta.cosma@unipd.it](mailto:marta.cosma@unipd.it)

### **ABSTRACT**

Low rates of lateral migration (centimetres to decimetres per year) combined with relatively high rates of vertical accretion (millimetres to centimetres per year) recorded in microtidal channels of the Venice Lagoon (Italy) give rise to point-bar geometries and internal facies arrangements that differ substantially from widely accepted models of point-bar sedimentary architecture. In this study, field data from the Venice Lagoon are combined with a three-dimensional forward stratigraphic model, the 'Point-Bar Sedimentary Architecture Numerical Deduction' (PB-SAND), to predict the stratal geometries of point bars formed in aggradational settings. The PB-SAND uses a combined geometric and stochastic modelling approach that can be constrained by field evidence. The model applied determines the geometry of four point bars generated by 9 to 11 m wide channels cutting through salt marshes. An iterative best-fit modelling approach has been used to obtain multiple simulations for each case-study, each of which fits the observations derived from the analysis of time-series historical aerial photographs and 44 sedimentary cores. Results demonstrate how the geometry of the bars is determined by the development of two key stratal surfaces: the point-bar brink and channel-thalweg surfaces. These surfaces are defined by the progressive translation and vertical shift of the point-bar brink (i.e. break of slope between bar top and bar slope) and the channel thalweg (i.e. deepest part of the channel) during bar evolution. The approach is used to: (i) reconstruct three-dimensional point-bar geometries; (ii) propose alternative reconstructions; (iii) provide insight to drive the acquisition of additional data to better constrain the proposed models; and (iv) provide insight into the mechanism of bar

growth for slowly migrating channels in settings subject to relatively high rates of aggradation. This study highlights how interaction between styles of planform transformation and latero-vertical shifts of meandering channels can determine the geometry of related sedimentary bodies.

**Keywords:** Aggradation, channel-thalweg trajectory, point-bar brink trajectory, tidal meanders, Venice Lagoon

## INTRODUCTION

The influence of vertical aggradation in shaping point-bar bodies is commonly considered to be negligible with respect to lateral migration processes. Hence, point bars are commonly described as purely laterally accreting bodies (e.g. Fisk, 1944; McGowen & Garner, 1970; Bridges & Leeder, 1976; Jackson, 1976; Miall, 1985; Smith, 1987; Durkin *et al.*, 2015; Colombera *et al.*, 2017) in which the point-bar brink (i.e. the break between bar top and bar slope, ideally approximated by the projection of the channel bankfull elevation on the inner bank) and the channel thalweg (i.e. the curve tracing the deepest part of the channel) shift towards the channel outer bank, generating point-bar bodies with an approximately tabular geometry. However, studies that document the lateral and vertical shift of both the point-bar brink and channel thalweg (De Mowbray, 1983; Nanson & Croke, 1992; Makaske, 2001; Rajchl & Uličný, 2005; Rieu *et al.*, 2005; Ghinassi *et al.*, 2014; Fielding, 2015; Ielpi *et al.*, 2015; Brivio *et al.*, 2016; Candel *et al.*, 2017; Boaga *et al.*, 2018; Finotello *et al.*, 2018a; Cosma *et al.*, 2019), suggest that, where the rate of aggradation is high (for example, millimetres to centimetres per year) relative to the rate of lateral channel migration (for example, centimetres to decimetres per year), geometries of resulting point-bar bodies can differ substantially from those of classical tabular sedimentary bodies. Development of point-bar geometries, and their internal stratal architectures, are also influenced by the different styles of bar planform evolution (Willis & Tang, 2010; Ghinassi *et al.*, 2013, 2016; Yan *et al.*, 2017; Willis & Sech, 2019a). However, even though the planform transformations of meander bends (i.e. expansion, rotation, translation and combinations thereof) are well-known (Daniel, 1971; Brice, 1974; Jackson, 1976; Nicoll & Hickin, 2010), the relationships between these transformations and resulting sediment-body architecture remains relatively under-explored (Ghinassi *et al.*, 2014; Durkin *et al.*, 2015; Johnston & Holbrook, 2018; Russell *et al.*, 2019). It follows that only a precise understanding of the interplay between planform transformation, spatio-temporal changes in channel hydraulic geometry and vertical shifts of the channel

system can reveal the effective three-dimensional geometry of point-bar bodies. Prior studies of modern migratory channels and ancient deposits have not yet comprehensively addressed this issue. Scroll-bar patterns of modern meanders provide clear evidence for their planform transformations, but related deposits are usually known only through one-dimensional or two-dimensional data from core and geophysical analysis (e.g. Bridge *et al.*, 1995; Clift *et al.*, 2018). On the contrary, the stratigraphic record provides a good control on the bar architecture, but in most cases the history of channel planform evolution is not evident. Exceptions to this are in cases where 3D seismic data (e.g. Smith *et al.*, 2009; Musial *et al.*, 2011) or rare planform exposures combined with vertical cliffs of ancient outcropping successions (e.g. Ielpi & Ghinassi, 2014; Bhattacharyya *et al.*, 2015; Ghinassi & Ielpi, 2015; Wu *et al.*, 2015; Swan *et al.*, 2019) are available.

Numerical models have contributed to current understanding of point-bar deposits resulting from interaction between planform and vertical styles of channel shifts (e.g. van de Lageweg *et al.*, 2016). Such models demonstrate how vertical aggradation influences the interconnectivity of coarse-grained deposits (i.e. channel lag or lower bar deposits) of adjacent bar bodies (Willis & Tang, 2010; Willis & Sech, 2019b), with notable implications for hydrocarbon recovery. Nevertheless, it is difficult to capture the complex interactions between flow dynamics, sediment transport, bank erosion and bar formation without the need to: (i) develop an extremely intricate model, which is highly demanding in computational terms; else (ii) rely upon a simplistic model, which has poor applicability to real-case examples.

The Point-Bar Sedimentary Architecture Numerical Deduction (PB-SAND) is a forward stratigraphic model (Yan *et al.*, 2017; Colombera *et al.*, 2018; Yan *et al.*, 2018, 2020) that uses input on channel planform and facies, together with current understanding of relations between meander-bend planform evolution and facies organization, to predict the three-dimensional architecture arising from the evolution of point-bar bodies in response to channel migration. The PB-SAND can be constrained by data from ancient deposits and modern systems (for example, remote sensing imagery, seismic data, cores and well logs). The PB-SAND is not process-oriented, and its input cannot be specified in terms of specific controlling factors on sedimentary processes; rather, it employs a primarily geometric-based modelling approach, which produces predictive three-dimensional architectural and facies-distribution models associated with specific planform evolution styles (Yan *et al.*, 2017). Values representative of certain types of point bars and their deposits are typically obtained from real-world datasets, held in a large

sedimentological database (cf. Colombera *et al.*, 2012, 2013). The geometric-based modelling approach allows the model to be applied to depict the expected form and behaviour of tidal meander bends and related point-bar deposits.

The PB-SAND is here parameterized with sedimentological evidence published by a recent study (Cosma *et al.*, 2019) from the Venice Lagoon (Italy), where tidal point bars have accreted in a depositional setting where the rate of aggradation (millimetres to centimetres per year) is high relative to the rate of lateral channel migration (centimetres to decimetres per year).

The aim of this study is to demonstrate the application of a novel method with which to better understand and explain the mutual role of lateral migration and vertical aggradation on meander dynamics and resultant point-bar stratal architecture. Four case studies of tidal meanders with variable bend geometries have been modelled to generate representations of the expected three-dimensional architecture of the accumulated point-bar bodies. Results from the analyses presented herein provide insight with which to better understand bar geometries generated by lateral channel shifts in highly aggradational depositional settings more generally (cf. Candel *et al.*, 2017), and of either tidal or fluvial origin. The specific objectives of this study are as follows: (i) to predict point-bar geometries developed under the active interplay between aggradation and planform transformation and define the three-dimensional expression of point-bar brink and channel-thalweg latero-vertical shifts; (ii) to discuss the results generated by the model in comparison with field evidence and establish type and amount of data required to confidently determine the 3D architecture of a bar; and (iii) to better understand the mechanism of bar growth in relatively high aggradational settings for which current point-bar models are not especially applicable.

## **GEOLOGICAL SETTING**

The Venice Lagoon, located along the northeastern coast of Italy (Fig. 1A), represents the largest brackish tidal basin of the Mediterranean Sea, with a longshore length and a width of *ca* 50 km and *ca* 10 km, respectively. It is a shallow microtidal basin, characterized by a mean water depth of tidal flats and subtidal platforms of *ca* 1.5 m and a semidiurnal tidal regime with an average range of *ca* 1.0 m. The lagoon is connected to the sea through three inlets: Lido, Malamocco and Chioggia (Fig. 1A).

The Venice Lagoon began to form about 7500 yr BP (Zecchin *et al.*, 2009) when the Holocene marine transgression (Amorosi *et al.*, 2008; Zecchin *et al.*, 2008, 2014) flooded the Venetian plain, a foreland basin comprised between the Apennine and South Alpine

chains (Massari *et al.*, 2009). After the Last Glacial Maximum (LGM), the northern Adriatic shelf was a low-gradient alluvial plain, dissected by an extensive network of fluvial channels. During the Holocene, the area was progressively flooded with the formation and drowning of barrier-lagoon systems located in progressively more landward positions (Trincardi *et al.*, 1994; Amorosi *et al.*, 2008; Storms *et al.*, 2008; Ronchi *et al.*, 2018). The lagoonal deposits, in the Venice area, are up to 20 m thick and consist of organic-rich mud with isolated sand bodies, which are mainly tidal or fluvio-tidal in origin (Madricardo *et al.*, 2007, 2012; Zecchin *et al.*, 2009, 2014; Madricardo & Donnici, 2014).

The present-day configuration of the lagoon is characterized by the presence of sparse salt marshes (Finotello *et al.*, 2020b) undergoing rapid erosion in the last two centuries (e.g. D'Alpaos, 2010; Tommasini *et al.*, 2019), wide subtidal platforms, and tidal flats that are cut by intertidal and subtidal channels (Finotello *et al.*, 2019; Ghinassi *et al.*, 2019) (Fig. 1A). In the north-eastern and south-western areas of the lagoon, there are salt marshes that occur at *ca* 5 to 50 cm above the mean sea level (Silvestri *et al.*, 2005; Roner *et al.*, 2016, 2017). Their accumulation has kept pace with the increasing rates of relative sea-level rise through organic and inorganic accumulation (e.g. D'Alpaos & Marani, 2016). In the 20<sup>th</sup> Century, salt-marsh accretion rates were about 0.07 to 0.66 cm/yr and 0.03 to 1.50 cm/yr in the northern (Bellucci *et al.*, 2007) and southern (Bellucci *et al.*, 2007; Roner *et al.*, 2017) lagoon, respectively.

The present study focuses on point-bar deposits associated with tidal meander bends located in the northern (Cases 1 and 2, Fig. 2C, D and E) and southern (Cases 3 and 4, Fig. 2B, F and G) Venice Lagoon (Cosma *et al.*, 2019). The meander bends are formed by intertidal channels that are 9 to 11 m wide and 0.5 to 1.8 m deep. Their radius of curvature ranges between 11 m and 29 m, and all the study channels show a 'simple symmetric' (*sensu* Brice, 1974) planform geometry. Channel bottoms are under 0.1 to 0.3 m of water at the lowest tide, whereas up to 0.5 m of water can cover overbank marshes at the highest tides.

## **DATA, METHODS AND TERMINOLOGY**

### **Remote sensing and field data**

Morphological characterization and reconstruction of the history of planform evolution of the studied meanders was undertaken by analysing and comparing historical aerial photographs (1955, 1968 and 1969) with satellite images acquired in 2014 via Google Earth®. Aerial photographs and satellite images were georeferenced using ArcGIS 10.4 (Esri, Redlands, CA, USA) with an accuracy of *ca* 1.0 m and *ca* 0.5 m, respectively. Superimposition of the temporally distinct images allowed quantitative evaluation of the lateral shifts of the studied channel bends (Finotello *et al.*, 2020a). Radiometrically constrained aggradation rates for the study areas were obtained from published data (Bellucci *et al.*, 2007; Roner *et al.*, 2017).

A total of 44 sedimentary cores, each up to 3.0 m deep, were recovered from the different point bars (Fig. 2). The location and spacing of the cores were limited by the site accessibility. For case study 3, cores were recovered only along the axis of the bar (Fig. 2E). For case studies 1 and 4, two additional cores were recovered along the inner bank in a seaward and landward position with respect to the bend apex (Fig. 2A and G). Finally, for case study 2, additional cores were recovered along four radial transects (Fig. 2C). The position of the cores was determined using differential GPS TOPCON GR-3 receivers (Topcon Positioning Systems Inc., Livermore, CA, USA) – dual frequency (L1/L2) and dual constellation NavStar/Glonass with integrated Tx/Rx UHF radio. To prevent sediment compaction, cores were recovered using an Eijkelkamp hand auger, with a 1.0 m long gouge sampler which has a diameter of 30 mm. Core sediment samples were kept humid in PVC liners, and then cut longitudinally, photographed and measured following basic principles of facies analyses. Particular attention was paid to the identification of features that could represent the preserved expression of the point-bar brink and the channel-thalweg zones in the cored sediments. The point-bar brink (Fig. 3) was placed where the inclination of the laminae changed from horizontal (i.e. bar-top deposits) to inclined (i.e. bar-slope deposits). Uncertainty associated with placement of the bar brink position was  $\pm 5$  cm (vertically in the cores), due to the gradual nature of the change in the inclination of the laminae. By contrast, the channel thalweg (Fig. 3) was precisely placed and corresponded to the erosional surface directly underlying the channel-lag deposits. Lateral correlation between adjacent cores was used to reveal 2D point-bar cross-sections along different transects, and for which point-bar brink and

channel-thalweg trajectories (Fig. 3) were defined based on shifts in position and elevation of point-bar brink and channel thalweg, respectively (*sensu* Brivio *et al.*, 2016). In sedimentary geology, the migratory behaviour of recognizable geomorphological features (for example, slope breaks) through space and time is sometime formalized through the definition of 'trajectories' (Helland-Hansen & Hampson, 2009). The trajectory concept has been widely applied to shelf edges and shorelines to understand distribution of depositional systems in response to relative sea-level change and variations in sediment supply (Henriksen *et al.*, 2009, and references therein), but it has also provided useful insight when applied to sedimentary bodies, like deltas (Gobo *et al.*, 2015; Cosgrove *et al.*, 2018) and fluvial bars (Ghinassi *et al.*, 2014). The concept of trajectory analysis is applied here to the point-bar brink and the channel thalweg of intertidal point bars to elucidate the possible architecture of deposits produced by meandering tidal channels in relatively high-aggradational settings.

### **Numerical modelling**

An iterative best-fit modelling approach has been used to create different realizations for each case study, based on the comparison with the observation derived from the analysis of aerial photographs and cores. The PB-SAND is a forward numerical model which employs a dominantly geometric-based modelling approach, supported by stochastic-based and process-based techniques, to model the sedimentary architecture of point bars and meander belts (Yan *et al.*, 2017). The model uses vector-based and grid-free algorithms. The PB-SAND enables the simulation of different meander-bend transformation behaviours (expansion, translation, rotation and combinations thereof) and of associated sedimentary facies distributions under different conditions of channel-system aggradation. Being a product-oriented numerical model, PB-SAND can be readily applied to tidal meanders and point bars. A brief overview of the model is provided below; a more detailed description of the modelling framework is provided by Yan *et al.* (2017). The forward stratigraphic modelling of point bars using PB-SAND is performed in two steps (Fig. 4): first, the planform evolution of the study meander is simulated; second, the geometry and distribution of sedimentary facies are modelled along cross-sections in any direction. The user controls these two steps through a series of input parameters, summarized in Fig. 4. In particular, the point-bar planform evolution is determined by its evolutionary transformation style, by the positions of the channel centreline at significant



time steps during meander evolution (notably, at channel inception and at time steps associated with temporal transition from one planform transformation style to another), and by the number of channel centrelines that are required to simulate accretion between these key time steps. These centrelines, which are used to define accretion surfaces in 3D, are linearly interpolated from the input channel centrelines for the key time steps. Changing the number of centrelines being modelled determines the size and geometry of accretion packages in a certain portion of the point-bar body and of the sedimentary facies therein, since an accretion package is constrained by two consecutive centrelines. Likewise, the number of centrelines determines the temporal resolution of both the brink and thalweg trajectories. In PB-SAND bar accretion is simulated to take place under bankfull conditions: this means that point-bar accretion surfaces are placed along a profile that extends from the channel thalweg to the bankfull elevation, i.e. the channel top that ultimately determines the position of the bar brink in the model outputs. The internal anatomy of point-bar accretion packages is modelled during the follow-on modelling procedure, which constitutes the above-mentioned second step. The spatial distribution of facies is inherently linked to the transformation style of a meander. For example, it is possible to prescribe a transition between sandy point-bar deposits and muddy counter-point-bar deposits (Smith *et al.*, 2009; Ghinassi *et al.*, 2016; Durkin *et al.*, 2019). The PB-SAND can also incorporate types of facies variations that are commonly seen in point-bar deposits, such as fining-upward, fining-outward and fining-downstream trends.

Accretion packages are also constrained by the geometry of the channel (width and maximum bankfull depth) and by rate of aggradation (Fig. 4). Temporal variations in channel width and depth can be simulated deterministically, and these give rise to spatial variations in the anatomy of the point-bar body. The model is also capable of accounting for streamwise variations in channel bathymetry (i.e. pool and riffle zones), based on specified relative depths of riffle and pool areas, which themselves can vary as a function of channel sinuosity. In particular, a rate of increase in depth change between pool and riffle areas with increasing channel sinuosity can be specified as model input. Aggradation is modelled through the progressive vertical offset of the channel, which translates to increases in the relative elevation of the point-bar packages at each time step, and can follow a linear behaviour or any other specified trend (Yan *et al.*, 2020).

Modelled point bars are populated with different sedimentary facies. Constraints set by the user include: (i) definition of the different lithofacies (as informed by the sediment cores); (ii) the proportion and vertical succession of facies (again informed by the cores); (iii) the spatial variation of facies with respect to the different planform transformation types (i.e. expansion, translation, rotation or combinations thereof); and (iv) the shape of bounding surfaces defining changes in facies or lithology within and across accretion packages (Fig. 4).

### **Terminology**

The terminology adopted in the present paper to refer to the different descriptive elements of tidal meander bends is reported in Fig. 3, and follows the terminology used for fluvial point bars, with some modifications that have been introduced in consideration of the bidirectional nature of tidal currents.

The terms point-bar brink and channel-thalweg trajectories were used in earlier articles to define the lateral and vertical shift of these two geomorphological elements along 2D vertical cross-sections (cf. Brivio *et al.*, 2016; Finotello *et al.*, 2018b; Cosma *et al.*, 2019). In the present study, this concept is developed into a three-dimensional perspective (Fig. 5). Two surfaces can be traced that represent the 3D envelopes of the positions occupied through time by the channel thalweg and by the point-bar brink, respectively; the difference in their vertical elevation corresponds to the thickness of the set of lateral-accretion packages forming the point-bar deposits (Fig. 5). The ratio between the magnitude of lateral shift and the magnitude of vertical aggradation of the bar brink zone will determine the geometry of the surface capping the bar, which is herein named the brink surface, and which is covered by overbank (salt-marsh) deposits (Fig. 5). A vertical cross-section through this surface (Fig. 5) defines the 2D point-bar brink trajectory (*sensu* Brivio *et al.*, 2016). Similarly, the ratio between the amounts of lateral and vertical shifts, either upward or downward, of the thalweg defines the geometry of the thalweg surface (Fig. 5), which corresponds to the base of the point-bar body. A vertical cross-section through the thalweg surface defines the 2D channel-thalweg trajectory (*sensu* Brivio *et al.*, 2016). Bar brink and thalweg trajectories are considered as apparent if the section is oblique to the true direction of channel shift (Fig. 5). The terms used to describe the shape of brink and thalweg trajectories, and of associated surfaces, are reported in Fig. 5. The term 'bend axis' is used to refer to the direction that is perpendicular to the tangent

to the apex of the bend and that passes through the apex. In cross-sections parallel to the bend axis, trajectories are classified as ascending, descending or horizontal on the basis of their vertical shifts. Considering the temporal variation of the ratio between the rate of lateral shift and the rate of vertical aggradation, ascending and descending trajectories can be classified as linear or non-linear (concave or convex-upward). Trajectories from cross-sections that run perpendicular to the bend axis are classified as symmetrical and asymmetrical with respect to this axis (Fig. 5).

## **RESULTS**

A brief overview on the sedimentology of the studied point-bar deposits is followed by descriptions of the main results of each case study, which are separately presented for: (i) remote sensing and field data; and (ii) numerical modelling. Remote sensing and field data provide evidence of channel planform transformations, as revealed by historical aerial and satellite imagery, and of the point-bar brink and channel-thalweg trajectories, as revealed by core analyses. From Case 1 to Case 4, the amount and quality of information that can be extracted from remote-sensing and field-derived data become progressively more limited. The PB-SAND numerical modelling outputs are presented for different realizations that honour the available field data.

### **Studied deposits**

Four main types of deposits have been recognized in the studied successions: substrate, channel-lag, point-bar and salt-marsh deposits. A brief description and interpretation of each type of deposit can be found in Table 1. Additionally, muddy channel-fill deposits have been observed in case study 4, but difficulty in accessing this site prevented coring and detailed description of these deposits. The thickness of channel-fill muds is inferred to approximate the thickness of the related point-bar sediments. The sedimentological analysis has focused mainly on the identification of the bar brink and thalweg in core, since the main focus of this research is to relate point-bar geometry to the known history of aggradation and planform channel transformation. Further details on these deposits are provided by Cosma *et al.* (2019).

### **Case Study 1**

#### *Remote sensing and field data*

The comparison between the 1955 and 2014 aerial photographs (Figs 2A, 2B and 6A) shows that the bend expanded during this period, and that the channel width increased from 5 to 10 m. This expansion allowed the inner bank to shift laterally by *ca* 14 m. In 1955, the channel cut through a tidal flat (Fig. 2A), and in the following decades halophytic vegetation progressively colonized most of the area growing from the channel margins (Fig. 2B).

Bar brink and thalweg trajectories have been reconstructed along the axial cross-section through the analysis of seven cores (Fig. 6B). The bar brink depth progressively decreases from 0.3 m in the inner part of the bar to zero at the bar edge, portraying a linear ascending trajectory. The thalweg trajectory shows an initial descending shift, followed by a sub-horizontal shift (Fig. 6B). The point-bar thickness increases towards the present-day channel from 0.60 (core 1) to 1.26 m (core 6) (Fig. 6B). The bar thickness is *ca* 1.26 m in the landward side of the bar (core 8) and at the bar apex (core 6), and *ca* 1.90 m in the seaward side (core 9). This increase in bar thickness is probably associated with the presence of a confluence in correspondence of the core site in 1955 (Fig. 6A).

#### *Numerical modelling*

The two historical aerial photographs and the nine sedimentary cores provide robust evidence for reconstruction of the planform evolution of the bar and of the geometries of the related brink and thalweg surfaces. Running a single PB-SAND model was sufficient to successfully simulate the evolution of the bar, via expansion under the influence of a linear rate of aggradation (Fig. 6C). To obtain a thalweg trajectory that matches the available core data, the channel depth in the model was set to increase from 0.90 to 1.25 m. This realization accurately reproduced the geometries of the studied bar, along with brink and thalweg surfaces, which appear to show a symmetrical concavity. Consequently, the section parallel to the bend axis shows a linearly ascending bar brink trajectory (section b–b', Fig. 6C), whereas, the sections transverse to the bend axis show a symmetric concave geometry (sections d–d' and e–e' in Fig. 6C). The thalweg trajectory shows an initial marked descending shift followed by a horizontal shift (Fig. 6C).

## **Case Study 2**

#### *Remote sensing and field data*

The comparison between the 1968 and 2014 aerial photographs (Figs 2C, 2D and 7A) shows that the channel maintained a constant width while undergoing asymmetrical

expansion. The channel lateral shift varied along the bend; along the landward side of the bend, this shift ranged between *ca* 1.1 m and 2.5 m, whereas in the apex zone it was *ca* 3 to 4 m, decreasing to zero at the seaward inflection point (Fig. 7A).

The 23 cores analysed show that brink depths vary between 0.74 to 0.20 m from the bar top. The surface defined by the vertical and lateral shift of the brink has an asymmetrical shape with respect to the bend axis: the brink surface is deeper and sub-horizontal in the landward part of the bar, and it is shallower and ascending in the seaward part (Fig. 7B). Along the axial cross-section, the brink trajectory shows a linear ascending pattern (Fig.7C). Thalweg depths (Fig. 7B) vary from 2.20 to 1.38 m from the bar top. The shallowest thalweg depths are located in the innermost part of the bar. Moving radially away from this point towards the active channel, a general descending and then ascending trajectory trend is evident (Fig.7B). The descending and then ascending thalweg trajectory is also seen on the axial cross-section (Fig.7C). In the active channel, the thalweg depth varies from 1.00 to 1.80 m in the riffle and pool areas, respectively. The point-bar thickness varies from 0.64 to 1.70 m.

#### *Numerical modelling*

As bend expansion can occur in combination with multiple types of planform transformation (Jackson, 1976), three realizations were produced with PB-SAND to represent different scenarios (Fig. 7D): (i) pure expansion; (ii) expansion combined with seaward rotation; and (iii) expansion combined with translation. In all three realizations, a linear rate of aggradation was used. Channel depth has been increased markedly from 1.0 to 1.6 m, and then gradually from 1.6 to 1.7 m, to simulate the trajectory of the thalweg. The change in channel bathymetry from pools to riffles has been set as constant for each time step (and associated value of channel sinuosity), setting the minimum channel depth (at riffle) as 0.4 times smaller than the maximum channel depth (at pool). The resulting point-bar brink and thalweg trajectories are depicted in Fig. 7D, E and F (realizations 1 to 3).

In realization 1 (Fig. 7D), both brink and thalweg surfaces show symmetrical concavity. As a consequence, in sections parallel to the bend axis, brink trajectories rise linearly from the innermost part of the bar towards the active channel (sections a–a' to c–c' in Fig. 7D), and thalweg trajectories descend slightly and then ascend toward the active channel (sections a–a' to c–c' in Fig. 7D). Accordingly, in sections that are transverse to the bend

axis, both thalweg and brink trajectories show a symmetrical concave-upward geometry (sections d–d' to e–e' in Fig. 7D).

In realization 2 (Fig. 7E), the seaward rotational component makes brink and thalweg surfaces asymmetrical with respect to the bend axis. In the seaward side of the bar, the brink surface gradually rises toward the bar edge, whereas along the landward side, it is abruptly cut by the active channel which shifted toward the bar through rotational expansion.

In realization 3 (Fig. 7F), the combination of expansion with seaward translation produced erosion of the brink surface along the landward side of the bar, whereas in the seaward part of the bar a gradually ascending brink surface is preserved. Realizations 2 and 3 are considered to be the most realistic, because they better explain the asymmetry of the thalweg surfaces, together with the erosion of the brink surface along the landward side of the bar.

### **Case Study 3**

#### *Remote sensing and field data*

The 1969 and 2014 aerial photographs demonstrate no substantial variation in either the planform morphology of the bend or the channel width (Figs 2E, 2F and 8A), indicating an extremely low (millimetres to centimetres/year) migration rate.

Bar brink and thalweg trajectories have been reconstructed along the axial cross-section based on the analysis of five cores (Fig. 8B). The brink depth decreases from 1.10 m in the innermost part of the bar (core 2) to 0.35 m at the bar edge (core 4), delineating a concave-upward ascending trajectory. The thalweg trajectory shows an initial descending shift, which is followed by an ascending shift almost parallel to the brink trajectory (Fig. 8B). The point-bar thickness ranges between 1.0 m and 1.8 m.

#### *Numerical modelling*

Two contrasting PB-SAND realizations (realizations 1 and 2, Fig. 8C and D) produced geometries comparable with those documented in the axial section of the bar.

Realization 1 (Fig. 8C) is based on point-bar expansion with non-linear aggradation and channel deepening from 1.0 to 1.8 m. The resulting brink and thalweg surfaces are symmetrical with respect to the bend axis (cross-sections d–d' and e–e' in Fig. 8C). The brink surface displays a rather flat geometry in the inner part of the bar that rises markedly in proximity of the bar edge (cross-sections a–a' to c–c' in Fig. 8C). The

thalweg surface progressively descends and then ascends from the inner part of the bar towards the active channel (cross-sections a–a', b–b' and c–c', Fig. 8C).

In realization 2 (Fig. 8D), bend translation has been modelled assuming linear aggradation. The channel depth has been increased through time from 1.35 to 1.80 m, to match closely with core observations (Fig. 8B). The brink trajectory rises linearly, as seen in cross-sections c–c' and d–d' (Fig. 8D), whereas its upward concavity on the axial cross-section (section a–a' in Fig. 8D) reflects apparent rather than true inclination. The thalweg trajectory, in the same direction, sharply descends and then gradually ascends towards the active channel (cross-sections c–c' and d–d', Fig. 8D). The available field evidence does not allow determination of which of these two realizations matches more closely the spatio-temporal evolution of the bar.

#### **Case Study 4**

##### *Remote sensing and field data*

The comparison between the 1955 and 2014 aerial photographs indicates that the study channel was captured by a larger channel, located towards the north-west (Fig. 2G and H). This capture triggered the silting of the channel, causing its progressive shallowing to the present-day depth (50 cm). However, the meander did not undergo any relevant planform change since the capture event, having maintained a constant width of *ca* 11 m (Figs 2G, 2H and 9A) through time.

The analysis of the five cores along the bend axis shows that the brink depth progressively diminishes from 1.94 m in the innermost part of the bar (core 1) to 0.30 m at the bar edge (core 4), creating a steep convex-upward ascending trajectory. The thalweg trajectory records an initial descending shift, which is followed by an ascending shift almost parallel to the brink trajectory (Fig. 9B). A final vertical rise of the thalweg trajectory records the progressive silting up of the channel, which is nowadays almost completely filled with sediments. The point-bar thickness increases from 2.0 to 2.5 m in the axial section, but no relevant changes in thickness are shown by cores from the riffle areas.

##### *Numerical modelling*

Three different PB-SAND realizations (realizations 1 to 3 in Fig. 9C, D and E) have been used to reconstruct possible geometries documented in the axial section, based on the following assumptions: (i) pure expansion under non-linear aggradation; (ii) expansion

with rotation under non-linear aggradation; and (iii) expansion followed by translation under linear aggradation. The channel depth has been increased through time from 1.30 to 2.25 m in realizations 1 and 3, and from 1.10 to 2.50 m in realization 2, respectively, to simulate the trajectory of the thalweg. In-channel silting, which resulted in aggradation and therefore determined a final vertical shift of the thalweg, has not been simulated by the model, since this process was not associated with contemporaneous point-bar growth (Fig. 9).

Realization 1 (Fig. 9C) yields brink and thalweg surfaces that are symmetrical with respect to the bend axis (cross-sections d–d' and e–e', Fig. 9C). Along axial cross-sections, the brink follows a convex-upward trajectory from the innermost part of the bar towards the active channel, whereas the thalweg trajectory, after an initial descending shift, rises almost parallel to the brink trajectory (cross-sections a–a', b–b' and c–c', Fig. 9C).

In realization 2 (Fig. 9D), resulting surfaces are asymmetrical with respect to the bend axis, and are much steeper in the seaward side of the bar (cross-sections d–d' and e–e' in Fig. 9D) in response to a rotational component during overall planform expansion. In sections parallel to the bend axis, the brink shows a convex-upward trajectory, whereas the thalweg trajectory, after an initial descending shift, rises almost parallel to the brink trajectory (cross-sections a–a', b–b' and c–c', Fig. 9D).

Realization 3 (Fig. 9E) yields brink and thalweg surfaces that are strongly asymmetrical with respect to the bend axis (cross-sections d–d' and e–e', Fig. 9E). The brink trajectory along the axial cross-section (cross-section b–b', Fig. 9E) shows a convex-upward trend, whereas the thalweg trajectory shows an initial descending direction followed by an approximately linear ascending trend (cross-sections of Fig. 9E). The paucity of field evidence for this bar precludes determination of which of these three realizations represents the most likely evolutionary history for this meander.

## **DISCUSSION**

The accretion geometries of point-bar bodies (Fig. 10) are classically represented on bend-axis sections as displaying a horizontal brink trajectory and thalweg trajectories that are either horizontal or slightly descending because of the local deepening at the pool zone of meander bends (Willis & Tang, 2010). In the present study, point-bar bodies are



documented in which the interplay between vertical aggradation and lateral migration has resulted in accretion geometries and brink and thalweg trajectories that differ from those depicted in traditional facies models for point-bar deposits (Fig. 10).

### **Point-bar brink and channel thalweg: From 2D trajectories to 3D surfaces**

In case studies 1 to 4, point-bar brink and channel-thalweg trajectories show different geometries, which can be classified as ascending, descending or horizontal in cross-sections parallel to the meander-bend axis. Point-bar brink trajectories are all ascending (Figs 6B, 7C, 8B and 9B) because the brink shift is caused by vertical aggradation. Brink trajectories can be classified as linear (Cases 1 and 2, Figs 6B and 7C) or non-linear (Cases 3 and 4, Figs 8B and 9B), depending on the variations in the ratio between vertical and lateral shifts of the brink. This ratio is constant in linear trajectories (Fig. 11B), and increases and decreases (Fig. 11B) for non-linear concave-upward (Case 3) and convex-upward (Case 4) trajectories, respectively. Thus, where aggradation increases relative to lateral migration for a given direction, trajectories will display a concave-upward pattern along that direction; the opposite applies to convex-upward trajectories. Channel-thalweg trajectories may include an initial descending shift, followed by an ascending or horizontal shift (Figs 7B and 8B). An increase of bend sinuosity typically results in thalweg deepening at the bend apex (Willis & Tang, 2010), whereas descending, ascending and horizontal shifts of the channel thalweg can variably occur in order to reach and maintain a depth that is in equilibrium with the channel discharge (Allen, 2000; D'Alpaos *et al.*, 2005). Additionally, thalweg trajectories can diverge, converge or remain parallel to the ascending brink trajectories (i.e. under aggradational conditions), indicating that the channel base shifted laterally under increasing, decreasing or stable discharge conditions, respectively (De Mowbray, 1983; Rieu *et al.*, 2005; Cosma *et al.*, 2019). Channel discharge is related to the tidal watershed area, and can vary over temporal scales of decades to centuries as a consequence of changes in the tidal prism and evolution of the channel network (Garofalo, 1980; Dalrymple *et al.*, 1991; Allen, 2000; D'Alpaos *et al.*, 2005; Stefanon *et al.*, 2012; Lanzoni & D'Alpaos, 2015; Ghinassi *et al.*, 2018a; b), including meander cut-off and capture events (for example, discharge decline caused by channel capture in case study 4, Fig. 9).

Trajectory analyses in cross-sections demonstrate how changes in depositional (for example, aggradation rate) and hydraulic (for example, discharge) conditions occurred

during the evolution of a meander bend, and observations of linear and non-linear geometries can be used to demonstrate variations in the ratio between vertical and lateral shifts (Cosma *et al.*, 2019). The numerical modelling realizations provide effective 3D geometries of surfaces generated by brink (i.e. brink surface) and thalweg (i.e. thalweg surface) shifts. The numerical modelling exercises undertaken for this study reveal that 2D trajectory analyses are more readily interpretable if conducted on sections that are oriented parallel to the effective direction of channel migration (i.e. are true trajectories, Figs 5 and 11C), since in this case the trajectories demonstrate the role of planform transformation in controlling geometries of brink and thalweg surfaces (Fig. 11A). On the contrary, sections oblique to the direction of channel migration provide only apparent trajectories (Fig. 5), which are not accurate descriptions of the effective relation between rates of vertical and lateral shifts. For example, the concave-upward geometry of the brink trajectory along the axial cross-section in Case 3 is obtained both in realization 1 (i.e. expansion with non-linear aggradation) and realization 2 (i.e. translation with linear aggradation). Nevertheless, the upward concavity of realization 2 is apparent, and arises from oblique orientation of the cross-section in comparison with direction of bar accretion. Understanding the three-dimensionality of the brink surface can also aid reconstructions of the planform transformations of the meander bend (Fig. 11A). Reconstruction of the brink surface steepness in different parts of the bar (i.e. shape of the brink surface) is crucial for distinguishing between symmetrical or asymmetrical bend growth. A steep brink surface is indicative of zones affected by pivoting processes, as commonly seen where bar rotation causes a local minimal lateral shift during vertical aggradation. A sub-vertical brink surface accounts for shift of the channel against the bar, as occurs in cases of translation or strong rotation (Fig. 11A). For these reasons, the asymmetrical shape of the brink surface of Case 2 is considered to be consistent with a non-uniform expansion (realizations 2 and 3); in contrast, pure expansion (realization 1) generated a symmetrical brink surface.

The analysis of point-bar brink and channel-thalweg surfaces can yield relevant insights in the evolution of ancient channel systems and help predict geometries of associated sedimentary bodies (Fig. 12). Different styles of planform evolution can occur under a variable ratio between lateral shift and vertical aggradation of channels, giving rise to a wide spectrum of combinations, which can influence the thickness of channel-belt

deposits (Willis & Sech, 2019a), and the morphology of their basal and top surfaces (Ghinassi *et al.*, 2016). Latero-vertical shift of channels controls geometry of point-bar bodies, along with inter-bar connectivity (Colombera *et al.*, 2017; Willis & Sech, 2019b), especially where aggradation allows adjacent bar bodies to overlap. Nevertheless, understanding the behaviour of brink and thalweg surfaces in the rock record is more challenging because of the effect of sediment-compaction processes, especially where fine-grained sediments dominate. Future research could focus on a reappraisal of ancient point-bar geometries through a detailed decompaction procedure at lithofacies scale (e.g. Hammer *et al.*, 2012; Li *et al.*, 2020).

### **Model evaluation**

Reconstruction of the effective three-dimensional architecture of modern tidal point-bar bodies is required to produce realistic facies models. Nevertheless, such a reconstruction is challenging, since understanding the evolution of tidal-bar planform morphology is commonly hindered by the lack of well-developed scroll-bar topographies (Hughes, 2012) and by low bend-migration rates (i.e. centimetres to decimetres per year; Garofalo, 1980; Gabet, 1998; Allen, 2000; Fagherazzi & Sun, 2004; Hughes, 2012; D'Alpaos *et al.*, 2017; Finotello *et al.*, 2018a), which makes comparison between historical photographs unfeasible (for example, Cases 3 and 4). Geophysical investigations are also unsuitable. Ground Penetrating Radar (GPR) is limited by the abundance of muddy sediments and salt water, which strongly attenuate GPR signal (Neal, 2004). Sub-bottom profilers (McClennen & Housley, 2006; Donnici *et al.*, 2017) cannot be used in subaerial settings and require water depths of at least 1 m. By necessity, reconstruction of bar geometries is therefore typically based on sedimentary cores and related 2D reconstructions.

The use of a forward stratigraphic model like PB-SAND allows prediction of the expected 3D internal architecture of these sedimentary bodies and provides an opportunity to consider multiple solutions, which can be used in combination with field-derived and time-series remote-sensing data to constrain the most likely evolutionary history of actively evolving point bars.

The range of presented case studies shows that where there exist sufficient constraints to unequivocally define both planform channel evolution (i.e. remote sensing and satellite images) and brink and thalweg trajectories (i.e. core data), PB-SAND can readily be applied to determine three-dimensional point-bar architectures that honour these

observations. This is demonstrated by Case 1, where a wealth of constraints provided by remote-sensing and core data could only be honoured fully by a single unique realization. In cases where field data provide only limited constraint, PB-SAND allows exploration of alternative competing possible models, and the evaluation of their likelihood given the available field evidence. This applies to Case 2, where two out of the three realizations were considered as plausible representations of bar geometry given the available field data. Where constraints are more limited (for example, Cases 3 and 4), alternative models show how contrasting styles of bar evolution can produce similar cross-sectional configurations (Fig. 11C). These models, in turn, provide information that can be used to plan further investigations (i.e. assisting in the identification of coring sites), and to constrain the bar geometry more effectively. The data needed to effectively constrain the model consist of at least two aerial photographs that reveal the temporal evolution of the channel planform morphology, and a set of cores collected along the direction of channel migration that reveal the true ratio between aggradation and lateral channel shift. With increasing complexity in the planform evolution of the channel system, due to the combination of different types of meander-bend transformation, the amount of data required to establish the geometry of the point-bar body increases.

## **CONCLUSIONS**

Data derived from remote-sensing and core analyses have been combined with the 'Point-Bar Sedimentary Architecture Numerical Deduction' (PB-SAND), a three-dimensional forward stratigraphic model, to reconstruct the stratal geometries of point-bar bodies formed by different meander bends in the aggradational marshes of the Venice Lagoon (Italy).

Field data reveal how the geometries of four studied bars, which differ from those depicted in traditional point-bar models, can be shaped in different ways by progressive lateral and vertical shifts of the brink and channel-thalweg zone. Integration of field data and numerical modelling demonstrates how cross-sections parallel to shift direction of the channels can show different shapes and steepness of point-bar brink and channel-thalweg trajectories. Ascending point-bar brink trajectories – which may be linear, concave or convex-upward – record different aggradational conditions during lateral channel shift. Descending thalweg trajectories document channel deepening, because of

temporal or streamwise bathymetric variations; horizontal to slightly rising shifts indicate limited change in channel cross-section. The PB-SAND can be used to reconstruct the three-dimensional architecture of a point-bar body unequivocally where the planform evolution of the bend, and the brink and thalweg trajectories are known. Moreover, PB-SAND simulations can demonstrate what combinations of different planform transformations and vertical aggradation can produce defined point-bar geometries along two-dimensional cross-sections. Where field data are insufficient to fully constrain a single 3D model, PB-SAND can render a series of possible alternative solutions, which can be used to plan further investigations.

## **ACKNOWLEDGEMENTS**

This work was supported by (i) HYDROSEM project (Progetto di Eccellenza CARIPARO 2017, Cassa di Risparmio Padova e Rovigo), “Fluvial and tidal meanders of the Venetian-Po Plain: from hydrodynamics to stratigraphy” (P.I. M. Ghinassi); and (ii) SID2016 project (University of Padova), “From channels to rock record: morphodynamic evolution of tidal meanders and related sedimentary products” (P.I. M. Ghinassi; prot. BIRD168939). NY, LC and NPM are grateful to AkerBP, Anadarko, Areva (now Orano), BHPBilliton, Cairn India [Vedanta], Chevron, ConocoPhillips, Equinor, Murphy Oil Corporation, Nexen-CNOOC, Occidental, Saudi Aramco, Shell, Tullow Oil, Woodside, and YPF for their financial support of the Fluvial & Eolian Research Group at the University of Leeds. NY, LC and NPM are also grateful to our project partner Petrotechnical Data Systems (PDS) for support. LC also gratefully acknowledges support by NERC (Catalyst Fund award NE/M007324/1 and Follow-on Fund award NE/N017218/1). The authors thank Chief Editor Ian Kane, Associate Editor Charlie Bristow, and reviewers Brian Willis and Catherine Russell for their thoughtful reviews, which have improved the article.

## **DATA AVAILABILITY STATEMENT**

The data that support the findings of this study are available from the corresponding author upon reasonable request.

## REFERENCES

- Allen, J.R.L.** (2000) Morphodynamics of Holocene salt marshes: a review sketch from the Atlantic and Southern North Sea coasts of Europe. *Quat. Sci. Rev.*, **19**, 1155–1231.
- Amorosi, A., Fontana, A., Antonioli, F., Primon, S. and Bondesan, A.** (2008) Post-LGM sedimentation and Holocene shoreline evolution in the NW Adriatic coastal area. *GeoActa*, **7**, 41–67.
- Bellucci, L.G., Frignani, M., Cochran, J.K., Albertazzi, S., Zaggia, L., Cecconi, G. and Hopkins, H.** (2007) <sup>210</sup>Pb and <sup>137</sup>Cs as chronometers for salt marsh accretion in the Venice Lagoon - links to flooding frequency and climate change. *J. Environ. Radioact.*, **97**, 85–102.
- Bhattacharyya, P., Bhattacharya, J.P. and Khan, S.D.** (2015) Paleo-channel reconstruction and grain size variability in fluvial deposits, Ferron Sandstone, Notom Delta, Hanksville, Utah. *Sediment. Geol.*, **325**, 17–25.
- Boaga, J., Ghinassi, M., D'Alpaos, A., Deidda, G.P., Rodriguez, G. and Cassiani, G.** (2018) Geophysical investigations unravel the vestiges of ancient meandering channels and their dynamics in tidal landscapes. *Sci. Rep.*, **8**, 1–8.
- Bondesan, A. and Meneghel, M.** (2004) Geomorfologia della provincia di Venezia. Note illustrative della carta geomorfologica della provincia di Venezia. 513 pp.
- Brice, J.C.** (1974) Evolution of meander loops. *Bull. Geol. Soc. Am.*, **85**, 581–586.
- Bridge, J.S., Alexander, J., Collier, R.E.L.L., Gawthorpe, R.L. and Jarvis, J.** (1995) Ground-penetrating radar and coring used to study the large-scale structure of point-bar deposits in three dimensions. *Sedimentology*, **42**, 839–852.
- Bridges, P.H. and Leeder, M.R.** (1976) Sedimentary model for intertidal mudflat channels, with examples from the Solway Firth, Scotland. *Sedimentology*, **23**, 533–552.
- Brivio, L., Ghinassi, M., D'Alpaos, A., Finotello, A., Fontana, A., Roner, M. and Howes, N.** (2016) Aggradation and lateral migration shaping geometry of a tidal point bar: An example from salt marshes of the Northern Venice Lagoon (Italy). *Sediment. Geol.*, **343**, 141–155.
- Candel, J.H.J., Makaske, B., Storms, J.E.A. and Wallinga, J.** (2017) Oblique aggradation: A novel explanation for sinuosity of low-energy streams in peat-filled

valley systems. *Earth Surf. Process. Landforms*, **42**, 2679–2696.

**Carniello, L., D'Alpaos, A. and Defina, A.** (2011) Modeling wind waves and tidal flows in shallow micro-tidal basins. *Estuar. Coast. Shelf Sci.*, **92**, 263–276.

**Carniello, L., Defina, A. and D'Alpaos, L.** (2009) Morphological evolution of the Venice lagoon: Evidence from the past and trend for the future. *J. Geophys. Res. Earth Surf.*, **114**, 1–10.

**Choi, K.S. and Jo, J.H.** (2015) Morphodynamics of Tidal Channels in the Open Coast Macrotidal Flat, Southern Ganghwa Island in Gyeonggi Bay, West Coast of Korea. *J. Sediment. Res.*, **85**, 582–595.

**Clift, P.D., Olson, E.D., Lechnowskyj, A., Moran, M.G., Barbato, A. and Lorenzo, J.M.** (2018) Grain-size variability within a mega-scale point-bar system, False River, Louisiana. *Sedimentology*, **66**, 408–434.

**Colombera, L., Mountney, N.P. and McCaffrey, W.D.** (2012) A relational database for the digitization of fluvial architecture. *Pet. Geosci.*, **18**, 129–140.

**Colombera, L., Mountney, N.P. and McCaffrey, W.D.** (2013) A quantitative approach to fluvial facies models: Methods and example results. *Sedimentology*, **60**, 1526–1558.

**Colombera, L., Mountney, N.P., Russell, C.E., Shiers, M.N. and McCaffrey, W.D.** (2017) Geometry and compartmentalization of fluvial meander-belt reservoirs at the bar-form scale: Quantitative insight from outcrop, modern and subsurface analogues. *Mar. Pet. Geol.*, **82**, 35–55.

**Colombera, L., Yan, N., McCormick-Cox, T. and Mountney, N.P.** (2018) Seismic-driven geocellular modeling of fluvial meander-belt reservoirs using a rule-based method. *Mar. Pet. Geol.*, **93**, 553–569.

**Cosgrove, G.I.E.E., Hodgson, D.M., Poyatos-Moré, M., Mountney, N.P. and McCaffrey, W.D.** (2018) Filter Or Conveyor? Establishing Relationships Between Clinof orm Rollover Trajectory, Sedimentary Process Regime, and Grain Character Within Intrashelf Clinothems, Offshore New Jersey, U.S.A. *J. Sediment. Res.*, **88**, 917–941.

**Cosma, M., Ghinassi, M., D'Alpaos, A., Roner, M., Finotello, A., Tommasini, L. and Gatto, R.** (2019) Point-bar brink and channel thalweg trajectories depicting interaction between vertical and lateral shifts of microtidal channels in the Venice Lagoon (Italy). *Geomorphology*, **342**, 37–50.

- D'Alpaos, A., Ghinassi, M., Finotello, A., Brivio, L., Bellucci, L.G. and Marani, M.** (2017) Tidal meander migration and dynamics: A case study from the Venice Lagoon. *Mar. Pet. Geol.*, **87**, 80–90.
- D'Alpaos, A., Lanzoni, S., Marani, M., Fagherazzi, S. and Rinaldo, A.** (2005) Tidal network ontogeny: Channel initiation and early development. *J. Geophys. Res. Earth Surf.*, **110**, 1–14.
- D'Alpaos, A. and Marani, M.** (2016) Reading the signatures of biologic-geomorphic feedbacks in salt-marsh landscapes. *Adv. Water Resour.*, **93**, 265–275.
- D'Alpaos, L.** (2010) Fatti e misfatti di idraulica lagunare. La laguna di Venezia dalla diversione dei fiumi alle nuove opere delle bocche di porto. *Istituto Veneto di Scienze, Lettere ed Arti*, Venice, 329 pp.
- Dalrymple, R.W., Makino, Y. and Zaitlin, B.A.** (1991) Temporal and spatial patterns of rhythmite deposition on mud flats in the macrotidal Cobequid Bay-Salmon River estuary. Bay of Fundy, Canada. In: *Clastic Tidal Sedimentology* (Ed. D.G. Smith, G.E. Reinson, B.A. Zaitlin, and R.A. Rahmani), 16, 137–160.
- Daniel, J.F.** (1971) Channel movement of meandering Indiana streams. *U.S. Geol. Surv. Prof. Pap.*, **732-A**, 1–18.
- De Mowbray, T.** (1983) The genesis of lateral accretion deposits in recent intertidal mudflat channels, Solway Firth, Scotland. *Sedimentology*, **30**, 425–435.
- Donnici, S., Madricardo, F. and Serandrei-Barbero, R.** (2017) Sedimentation rate and lateral migration of tidal channels in the Lagoon of Venice (Northern Italy). *Estuar. Coast. Shelf Sci.*, **198**, 354–366.
- Durkin, P.R., Hubbard, S.M., Boyd, R.L. and Leckie, D.A.** (2015) Stratigraphic Expression of Intra-Point-Bar Erosion and Rotation. *J. Sediment. Res.*, **85**, 1238–1257.
- Durkin, P.R., Hubbard, S.M., Smith, D.G. and Leckie, D.A.** (2019) Predicting heterogeneity in meandering fluvial and tidal-fluvial deposits: The point bar to counter point bar transition. In: *Fluvial Meanders and Their Sedimentary Products in the Rock Record* (Ed. M. Ghinassi, L. Colombera, N.P. Mountney, A.J. Reesink, and M. Bateman), *John Wiley & Sons, Ltd*, 231–249.
- Fagherazzi, S. and Sun, T.** (2004) A stochastic model for the formation of channel networks in tidal marshes. *Geophys. Res. Lett.*, **31**, 1–4.



- Fielding, C.R.** (2015) A reappraisal of large, heterolithic channel fills in the upper Permian Rangal Coal Measures of the Bowen Basin, Queensland, Australia: The case for tidal influence. In: *Fluvial-Tidal Sedimentology*, 1st edn. (Ed. P.J. Ashworth, J.L. Best, and D.R. Parsons), Elsevier B.V., 68, 323–351.
- Finotello, A., Canestrelli, A., Carniello, L., Ghinassi, M. and D’Alpaos, A.** (2019) Tidal flow asymmetry and discharge of lateral tributaries drive the evolution of a microtidal meander in the Venice Lagoon (Italy). *J. Geophys. Res. Earth Surf.*, **124**, 3043–3066.
- Finotello, A., Ghinassi, M., Carniello, L., Belluco, E., Pivato, M., Tommasini, L. and D’Alpaos, A.** (2020a) Three-dimensional flow structures and morphodynamic evolution of microtidal meandering channels. *Water Resour. Res.*, **56**, e2020WR027822.
- Finotello, A., Lanzoni, S., Ghinassi, M., Marani, M., Rinaldo, A. and D’Alpaos, A.** (2018a) Supporting Information (SI) Appendix. Field migration rates of tidal meanders recapitulate fluvial morphodynamics. *Proc. Natl. Acad. Sci.*, **115**, 1463–1468.
- Finotello, A., Lanzoni, S., Ghinassi, M., Marani, M., Rinaldo, A. and D’Alpaos, A.** (2018b) Field migration rates of tidal meanders recapitulate fluvial morphodynamics. *Proc. Natl. Acad. Sci.*, **115**, 201711330.
- Finotello, A., Marani, M., Carniello, L., Pivato, M., Roner, M., Tommasini, L. and D’alpaos, A.** (2020b) Control of wind-wave power on morphological shape of salt marsh margins. *Water Sci. Eng.*, **13**, 45–56.
- Fisk, H.N.N.** (1944) Geological Investigation of the Alluvial Valley of the Lower Mississippi River. *US Army Corps Eng. Mississippi River Comm.*, 1–78.
- Gabet, E.J.** (1998) Lateral Migration and Bank Erosion in a Saltmarsh. *Estuaries*, **21**, 745–753.
- Garofalo, D.** (1980) The Influence of Wetland Vegetation on Tidal Stream Channel Migration and Morphology. *Estuaries*, **3**, 258–270.
- Ghinassi, M., Billi, P., Libsekal, Y., Papini, M. and Rook, L.** (2013) Inferring Fluvial Morphodynamics and Overbank Flow Control From 3D Outcrop Sections of A Pleistocene Point Bar, Dandiero Basin, Eritrea. *J. Sediment. Res.*, **83**, 1065–1083.
- Ghinassi, M., Brivio, L., D’Alpaos, A., Finotello, A., Carniello, L., Marani, M. and**

- Cantelli, A.** (2018a) Morphodynamic evolution and sedimentology of a microtidal meander bend of the Venice Lagoon (Italy). *Mar. Pet. Geol.*, **96**, 391–404.
- Ghinassi, M., D'Alpaos, A., Gasparotto, A., Carniello, L., Brivio, L., Finotello, A., Roner, M., Franceschinis, E., Realdon, N., Howes, N. and Cantelli, A.** (2018b) Morphodynamic evolution and stratal architecture of translating tidal point bars: Inferences from the northern Venice Lagoon (Italy). *Sedimentology*, **65**, 1354–1377.
- Ghinassi, M., D'Alpaos, A., Tommasini, L., Brivio, L., Finotello, A. and Stefani, C.** (2019) Tidal currents and wind waves controlling sediment distribution in a subtidal point bar of the Venice Lagoon (Italy). *Sedimentology*, **66**, 2926–2949.
- Ghinassi, M. and Ielpi, A.** (2015) Stratal Architecture and Morphodynamics of Downstream-Migrating Fluvial Point Bars (Jurassic Scalby Formation, U.K.). *J. Sediment. Res.*, **85**, 1123–1137.
- Ghinassi, M., Ielpi, A., Aldinucci, M. and Fustic, M.** (2016) Downstream-migrating fluvial point bars in the rock record. *Sediment. Geol.*, **334**, 66–96.
- Ghinassi, M., Nemec, W., Aldinucci, M., Nehyba, S., Ozaksoy, V., Fidolini, F., Özaksoy, V. and Fidolini, F.** (2014) Plan-form evolution of ancient meandering rivers reconstructed from longitudinal outcrop sections. *Sedimentology*, **61**, 952–977.
- Gobo, K., Ghinassi, M. and Nemec, W.** (2015) Gilbert-type deltas recording short-term base-level changes: Delta-brink morphodynamics and related foreset facies. *Sedimentology*, **62**, 1923–1949.
- Hammer, E., Brandsegg, K.B., Mørk, M.B.E. and Næss, A.** (2012) Reconstruction of heterogeneous reservoir architecture based on differential decompaction in sequential re-burial modelling. *Pet. Geosci.*, **18**, 173–189.
- Helland-Hansen, W. and Hampson, G.J.** (2009) Trajectory analysis: Concepts and applications. *Basin Res.*, **21**, 454–483.
- Henriksen, S., Hampson, G.J., Helland-Hansen, W., Johannessen, E.P. and Steel, R.J.** (2009) Shelf edge and shoreline trajectories, a dynamic approach to stratigraphic analysis. *Basin Res.*, **21**, 445–453.
- Hughes, Z.J.** (2012) Tidal Channels on Tidal Flats and Marshes. In: *Principles of Tidal Sedimentology* (Ed. R.A. Davis and R.W. Dalrymple), *Springer*, 269–300.
- Ielpi, A. and Ghinassi, M.** (2014) Planform architecture, stratigraphic signature and morphodynamics of an exhumed Jurassic meander plain (Scalby Formation,

Yorkshire, UK). *Sedimentology*, **61**, 1923–1960.

**Ielpi, A., Gibling, M.R., Bashforth, A.R. and Dennar, C.I.** (2015) Impact of Vegetation on Early Pennsylvanian Fluvial Channels: Insight From the Joggins Formation of Atlantic Canada. *J. Sediment. Res.*, **85**, 999–1018.

**Jackson, R.G.I.** (1976) Depositional Model of Point Bars in the Lower Wabash River. *J. Sediment. Petrol.*, **46**, 579–594.

**Johnston, S. and Holbrook, J.** (2018) Toggling between expansion and translation. In: *Fluvial Meanders and Their Sedimentary Products in the Rock Record* (Ed. M. Ghinassi, L. Colombera, N.P. Mountney, A.J. Reesink, and M. Bateman), *John Wiley & Sons, Ltd*, 48, 47–80.

**Lanzoni, S. and D'Alpaos, A.** (2015) On funneling of tidal channels. *J. Geophys. Res. Earth Surf.*, **120**, 433–452.

**Li, W., Yue, D., Colombera, L., Mountney, N.P. and Wu, S.** (2020) A novel method for estimating sandbody compaction in fluvial successions. *Sediment. Geol.*, 105675.

**Madricardo, F. and Donnici, S.** (2014) Mapping past and recent landscape modifications in the Lagoon of Venice through geophysical surveys and historical maps. *Anthropocene*, **6**, 86–96.

**Madricardo, F., Donnici, S., Lezziero, A., De Carli, F., Buogo, S., Calicchia, P. and Boccardi, E.** (2007) Palaeoenvironment reconstruction in the Lagoon of Venice through wide-area acoustic surveys and core sampling. *Estuar. Coast. Shelf Sci.*, **75**, 205–213.

**Madricardo, F., Tegowski, J. and Donnici, S.** (2012) Automated detection of sedimentary features using wavelet analysis and neural networks on single beam echosounder data: A case study from the Venice Lagoon, Italy. *Cont. Shelf Res.*, **43**, 43–54.

**Makaske, B.** (2001) Anastomosing rivers: A review of their classification, origin and sedimentary products. *Earth Sci. Rev.*, **53**, 149–196.

**Massari, F., Grandesso, P., Stefani, C. and Jobstraibizer, P.G.** (2009) A small polyhistory foreland basin evolving in a context of oblique convergence: the Venetian basin (Chattian to Recent, Southern Alps, Italy). In: *Foreland Basins* (Ed. P.A. Allen and P. Homewood), *Blackwell Scientific*, Oxford, 141–168.

**McClennen, C.E. and Housley, R.A.** (2006) Late-Holocene Channel Meander Migration

and Mudflat Accumulation Rates, Lagoon of Venice, Italy. *J. Coast. Res.*, **22**, 930–945.

- McGowen, J.H.** and **Garner, L.E.** (1970) Physiographic Features and Stratification Types of Coarse-Grained Pointbars: Modern and Ancient Examples. *Sedimentology*, **14**, 77–111.
- Miall, A.D.** (1985) Architectural-element analysis: A new method of facies analysis applied to fluvial deposits. *Earth-Science Rev.*, **22**, 261–308.
- Musial, G., Reynaud, J.Y., Gingras, M.K., Féliès, H., Labourdette, R. and Parize, O.** (2012) Subsurface and outcrop characterization of large tidally influenced point bars of the Cretaceous McMurray Formation (Alberta, Canada). *Sediment. Geol.*, **279**, 156–172.
- Nanson, G.C.** and **Croke, J.C.** (1992) A genetic classification of floodplains. *Geomorphology*, **4**, 459–486.
- Neal, A.** (2004) Ground-penetrating radar and its use in sedimentology: principles, problems and progress. *Earth Sci Rev.* doi: 10.1016/j.earscirev.2004.01.004
- Nicoll, T.J.** and **Hickin, E.J.** (2010) Planform geometry and channel migration of confined meandering rivers on the Canadian prairies. *Geomorphology*, **116**, 37–47.
- Rajchl, M.** and **Uličný, D.** (2005) Depositional record of an avulsive fluvial system controlled by peat compaction (Neogene, Most Basin, Czech Republic). *Sedimentology*, **52**, 601–625.
- Rieu, R., van Heteren, S., van der Spek, A.J.F. and De Boer, P.L.** (2005) Development and preservation of a Mid-Holocene tidal-channel network offshore the Western Netherlands. *J. Sediment. Res.*, **75**, 409–419.
- Ronchi, L., Fontana, A., Correggiari, A. and Asioli, A.** (2018) Late Quaternary incised and infilled landforms in the shelf of the northern Adriatic Sea (Italy). *Mar. Geol.*, **405**, 47–67.
- Roner, M., D’Alpaos, A., Ghinassi, M., Marani, M., Silvestri, S., Franceschinis, E. and Realdon, N.** (2016) Spatial variation of salt-marsh organic and inorganic deposition and organic carbon accumulation: Inferences from the Venice lagoon, Italy. *Adv. Water Resour.*, **93**, 276–287.
- Roner, M., Ghinassi, M., Fedi, M., Liccioli, L., Bellucci, L.G., Brivio, L., D’Alpaos, A. and D’Alpaos, A.** (2017) Latest Holocene depositional history of the southern

Venice Lagoon, Italy. *The Holocene*, **27**, 1731–1744.

- Russell, C.E., Mountney, N.P., Hodgson, D.M. and Colombera, L.** (2019) A novel approach for prediction of lithological heterogeneity in fluvial point-bar deposits from analysis of meander morphology and scroll-bar pattern. In: *Fluvial Meanders and Their Sedimentary Products in the Rock Record* (Ed. M. Ghinassi, L. Colombera, N.P. Mountney, A.J. Reesink, and M. Bateman), *John Wiley & Sons, Ltd*, 385–417.
- Silvestri, S., Defina, A. and Marani, M.** (2005) Tidal regime, salinity and salt marsh plant zonation. *Estuar. Coast. Shelf Sci.*, **62**, 119–130.
- Smith, D.G.** (1987) Meandering river point bar lithofacies models: modern and ancient examples compared. In: *Recent Developments in Fluvial Sedimentology: Contributions from the Third International Fluvial Sedimentology Conference* (Ed. F.G. Ethridge, R.M. Flores, and M.D. Harvey), *SEPM Society for Sedimentary Geology*, **39**, 83–91.
- Smith, D.G., Hubbard, S.M., Leckie, D.A. and Fustic, M.** (2009) Counter point bar deposits: lithofacies and reservoir significance in the meandering modern Peace River and ancient McMurray Formation, Alberta, Canada. *Sedimentology*, **56**, 1655–1669.
- Stefanon, L., Carniello, L., D’Alpaos, A. and Rinaldo, A.** (2012) Signatures of sea level changes on tidal geomorphology: Experiments on network incision and retreat. *Geophys. Res. Lett.*, **39**, 1–6.
- Storms, J.E.A., Weltje, G.J., Terra, G.J., Cattaneo, A. and Trincardi, F.** (2008) Coastal dynamics under conditions of rapid sea-level rise: Late Pleistocene to Early Holocene evolution of barrier–lagoon systems on the northern Adriatic shelf (Italy). *Quat. Sci. Rev.*, **27**, 1107–1123.
- Swan, A., Hartley, A.J., Owen, A. and Howell, J.** (2019) Reconstruction of a sandy point-bar deposit: implications for fluvial facies analysis. In: *Fluvial Meanders and Their Sedimentary Products in the Rock Record* (Ed. M. Ghinassi, L. Colombera, N.P. Mountney, A.J. Reesink, and M. Bateman), *John Wiley & Sons, Ltd*, 445–474.
- Terwindt, J.H.J.** (1988) Palaeotidal reconstructions of inshore tidal depositional environments. In: *Tide-Influenced Sedimentary Environments* (Ed. P.L. De Boer, A. van Gelder, and S.-D. Nio), 233–263.
- Tommasini, L., Carniello, L., Ghinassi, M., Roner, M. and D’Alpaos, A.** (2019)

Changes in the wind-wave field and related salt-marsh lateral erosion: inferences from the evolution of the Venice Lagoon in the last four centuries. *Earth Surf Process Landforms*. doi: 10.1002/esp.4599

- Trincardi, F., Correggiari, A. and Roveri, M.** (1994) Late Quaternary transgressive erosion and deposition in a modern epicontinental shelf: the Adriatic Semienclosed Basin. *Geo-Marine Lett.*, **14**, 41–51.
- van de Lageweg, W.I., Schuurman, F., Cohen, K.M., van Dijk, W.M., Shimizu, Y. and Kleinhans, M.G.** (2016) Preservation of meandering river channels in uniformly aggrading channel belts. *Sedimentology*, **63**, 586–608.
- Willis, B.J. and Sech, R.P.** (2019a) Emergent facies patterns within fluvial channel belts. In: *Fluvial Meanders and Their Sedimentary Products in the Rock Record* (Ed. M. Ghinassi, L. Colombera, N.P. Mountney, A.J. Reesink, and M. Bateman), *John Wiley & Sons, Ltd*, 509–542.
- Willis, B.J. and Sech, R.P.** (2019b) Quantifying impacts of fluvial intra-channel-belt heterogeneity on reservoir behaviour. In: *Fluvial Meanders and Their Sedimentary Products in the Rock Record* (Ed. M. Ghinassi, L. Colombera, N.P. Mountney, A.J. Reesink, and M. Bateman), *John Wiley & Sons, Ltd*, 543–572.
- Willis, B.J. and Tang, H.** (2010) Three-Dimensional Connectivity of Point-Bar Deposits. *J. Sediment. Res.*, **80**, 440–454.
- Wu, C., Bhattacharya, J.P. and Ullah, M.S.** (2015) Paleohydrology and 3D Facies Architecture of Ancient Point Bars, Ferron Sandstone, Notom Delta, South-Central Utah, U.S.A. *J. Sediment. Res.*, **85**, 399–418.
- Yan, N., Colombera, L. and Mountney, N.P.** (2020) Three-dimensional forward stratigraphic modelling of the sedimentary architecture of meandering-river successions in evolving half-graben rift basins. *Basin Res.*, **32**, 68–90.
- Yan, N., Colombera, L., Mountney, N.P. and Dorrell, R.M.** (2018) Fluvial point-bar architecture and facies heterogeneity and their influence on intra-bar static connectivity in humid coastal-plain and dryland fan systems. In: *Fluvial Meanders and Their Sedimentary Products in the Rock Record* (Ed. M. Ghinassi, L. Colombera, N.P. Mountney, A.J. Reesink, and M. Bateman), *John Wiley & Sons, Ltd*, 475–508.
- Yan, N., Mountney, N.P., Colombera, L. and Dorrell, R.M.** (2017) A 3D forward

stratigraphic model of fluvial meander-bend evolution for prediction of point-bar lithofacies architecture. *Comput. Geosci.*, **105**, 65–80.

**Zecchin, M., Baradello, L., Brancolini, G., Donda, F., Rizzetto, F. and Tosi, L.** (2008)

Sequence stratigraphy based on high-resolution seismic profiles in the late Pleistocene and Holocene deposits of the Venice area. *Mar. Geol.*, **253**, 185–198.

**Zecchin, M., Brancolini, G., Tosi, L., Rizzetto, F., Caffau, M. and Baradello, L.** (2009)

Anatomy of the Holocene succession of the southern Venice lagoon revealed by very high-resolution seismic data. *Cont. Shelf Res.*, **29**, 1343–1359.

**Zecchin, M., Tosi, L., Caffau, M., Baradello, L. and Donnici, S.** (2014) Sequence

stratigraphic significance of tidal channel systems in a shallow lagoon (Venice, Italy).

*The Holocene*, **24**, 646–658.

## FIGURE CAPTIONS

**Fig. 1.** Study sites. (A) Location of the Venice Lagoon along the north-eastern coast of Italy. (B) and (C) Location of the study sites in the northern (Cases 1 and 2) and southern (Cases 3 and 4) Venice Lagoon, respectively.

**Fig. 2.** Satellite images (left) and aerial photographs (right) used for remote sensing analysis. (A), (C), (E) and (G) Satellite images showing the studied meander bends in 2014. (B), (D), (F) and (H) Aerial photographs showing the bends in 1955 (Cases 1 and 4), 1968 (Case 2) and 1969 (Case 3). The yellow spots indicate the position of the recovered cores for each meander.

**Fig. 3.** Descriptive terminology for tidal meander bends and point-bar architecture. Point-bar brink and channel thalweg are sketched highlighting the main characteristics used to recognize them in sedimentary cores.

**Fig. 4.** 'Point-Bar Sedimentary Architecture Numerical Deduction' (PB-SAND) workflow: PB-SAND models the sedimentary architecture of point bars in two steps, reconstructing the planform evolution first, and then the geometry and distribution of sedimentary facies along cross-sections.

**Fig. 5.** Terminology used in the present work to describe point-bar brink and channel-thalweg three-dimensional surfaces and two-dimensional trajectories. An example of bar-brink surface and trajectories resulting from point-bar expansion is given (not to scale).

**Fig. 6.** Case 1 results. (A) and (B) Results from remote sensing and core analysis, showing the planform evolution of the meander bend (A) and bar-brink and channel-thalweg trajectories along the axial cross-section (B). (C) The PB-SAND modelling results of realization 1, showing the expansional evolution of the meander bend developed under linear aggradational conditions and the resultant three-dimensional geometry of the point bar. Vertical exaggeration: x2.

**Fig. 7.** Case 2 results. (A), (B) and (C) Results from remote sensing and core analysis, showing the planform evolution of the meander bend (A), bar-brink and channel-thalweg depths resulting from core analysis (B) and trajectories along the axial cross-section (C). (D), (E) and (F) The PB-SAND modelling results of realizations 1, 2 and 3, respectively, developed under linear aggradational conditions. (D) Realization 1: expansional evolution of the meander bend and three-dimensional geometry of the point bar. (E) Realization 2: expansional and rotational evolution of the meander bend and resultant three-



dimensional geometry of the point bar. (F) Realization 3: expansional and translational evolution of the meander bend and resultant three-dimensional geometry of the point bar. Vertical exaggeration: x2.

**Fig. 8.** Case 3 results. (A) and (B) Results from remote sensing and core analysis, showing the planform evolution of the meander bend (A) and bar-brink and channel-thalweg trajectories along the axial cross-section (B). (C) and (D) The PB-SAND modelling results of realizations 1 and 2, respectively. (C) Realization 1: expansional evolution of the meander bend developed under non-linear aggradational conditions and resultant three-dimensional geometry of the point bar. (D) Realization 2: translational evolution of the meander bend developed under linear aggradational conditions and resultant three-dimensional geometry of the point bar. Vertical exaggeration: x2.

**Fig. 9.** Case 4 results. (A) and (B) Results from remote sensing and core analysis, showing the planform evolution of the meander bend (A) and bar-brink and channel-thalweg trajectories along the axial cross-section (B). (C), (D) and (E) The PB-SAND modelling results of realizations 1, 2 and 3, respectively. (C) Realization 1: expansional evolution of the meander bend developed under non-linear aggradation and three-dimensional geometry of the point bar. (D) Realization 2: expansional and rotational evolution of the meander bend developed under non-linear aggradation and resultant three-dimensional geometry of the point bar. (E) Realization 3: expansional and translational evolution of the meander bend developed under linear aggradation and resultant three-dimensional geometry of the point bar. Vertical exaggeration: x2.

**Fig. 10.** Differences between traditional (A) and highly aggrading (B) point-bar models. (A) Geometries of the brink and thalweg surfaces resulting from an expansional evolution of the meander bend envisaged by traditional models. (B) Geometries of the brink and thalweg surfaces resulting from an expansional evolution of the meander bend developed under aggradational conditions.

**Fig. 11.** Summary of the main factors influencing point-bar geometries. (A) Brink surfaces resulting from different planform transformations. (B) Brink surfaces resulting from different aggradational conditions. (C) Combination of different planform transformations and aggradational conditions (linear versus non-linear) can produce similar cross-sectional configurations. However, only the cross-sections parallel to the effective direction of channel migration (I and III) offer a faithful reflection of the relationship









between vertical aggradation and lateral migration of the channel system. The examples reported herein are referred to the brink surface, but the same considerations can be made for the thalweg surface. Vertical exaggeration: x5.

**Fig. 12.** Summary model illustrating brink and thalweg trajectories of two channel-belt storeys developed under aggradational conditions and different planform transformations (storey 1: translation; storey 2: expansion).

#### **TABLE CAPTION**

**Table 1.** Deposits of the study sites. References for the interpretation: Terwindt (1988); Bondesan & Meneghel (2004); Silvestri *et al.* (2005); Carniello *et al.* (2009, 2011); Choi & Jo (2015).

Table 1

Description	Interpretation	Photographs	
<p>Overlying point bar and substrate deposits. Brownish, oxidized mud with 1 to 3 mm thick horizontal well-sorted sandy laminae, <i>in situ</i> roots, wood fragments and bioturbation. Maximum thickness ranges from 1.94 to 0.31 m. Along axial transects, thickness decreases toward the channel</p>	<p>Oxidation and root presence are indicative of frequent subaerial exposure (Silvestri <i>et al.</i>, 2005). Mud is deposited by fallout during high slack water. Sandy laminae sorting suggests winnowing of finer particles probably due to wave action during storm events</p>	 <p>horizontal laminae 1 cm</p>	 <p>roots 1 cm</p>
<p>Gradational lower and upper boundaries with channel lag and salt marsh deposits, respectively. From mud to fine sand clinostratified deposits up to 2.30 m thick. Frequently massive towards the base. More clear inclined heterolithic stratification towards the top with well-sorted very fine to fine sand or plant debris laminae dipping channelward between 5° to 25° alternating with mud. Laminae inclination decreases towards the top. Widespread bioturbation often prevents identification of sedimentary structures</p>	<p>Clinostratification points out the deposition of sediment as a consequence of channel lateral shift. In the heterolithic stratification, abundance of mud reflects the prevalence of fallout processes, probably related to slack water periods (Carniello <i>et al.</i>, 2011) while the well-sorted laminae are the result of entrainment of finer material probably due to wave-winnowing during storm events (Choi &amp; Jo, 2015). Decreasing of laminae inclination towards the top reflects bar slope topography</p>	 <p>bioturbation 1 cm</p>	 <p>inclined plant-debris laminae 1 cm</p>
<p>Erosionally overlying substrate deposits and grading upward toward point bar deposits. 5 to 20 cm thick massive layer of silt to medium sand. Shells, shell fragments, pebble-sized rounded mud clasts and plant debris are common</p>	<p>Deepest part of the channel with the erosional surface and the concentration of coarser sediments and shells. Pebble-sized mud clasts are formed by comminution of collapsed bank blocks (Terwindt, 1988)</p>	 <p>shells 1 cm</p>	 <p>mud clasts 1 cm</p>
<p>Two different types: (1) alternation of well-sorted medium to very fine sand layers and dark, organic-rich muddy layers with shell and plant debris fragments. Pervasive bioturbation prevents detection of sedimentary structures. (2) comminute dark brown to black plant debris with a minimum amount of dispersed mud with abundant reeds and reed fragments</p>	<p>(1) tidal flat/subtidal environment (Cases 1 and 2). Sandy layer formed because of wave-winnowing during storm events (Carniello <i>et al.</i>, 2009). Muddy layers settled from suspension during fair weather period. (2) peat deposits (Cases 3 and 4) consistent with wetland setting (Bondesan &amp; Meneghel, 2004)</p>	 <p>sandy substrate 1 cm</p>	 <p>peat substrate reeds 1 cm</p>

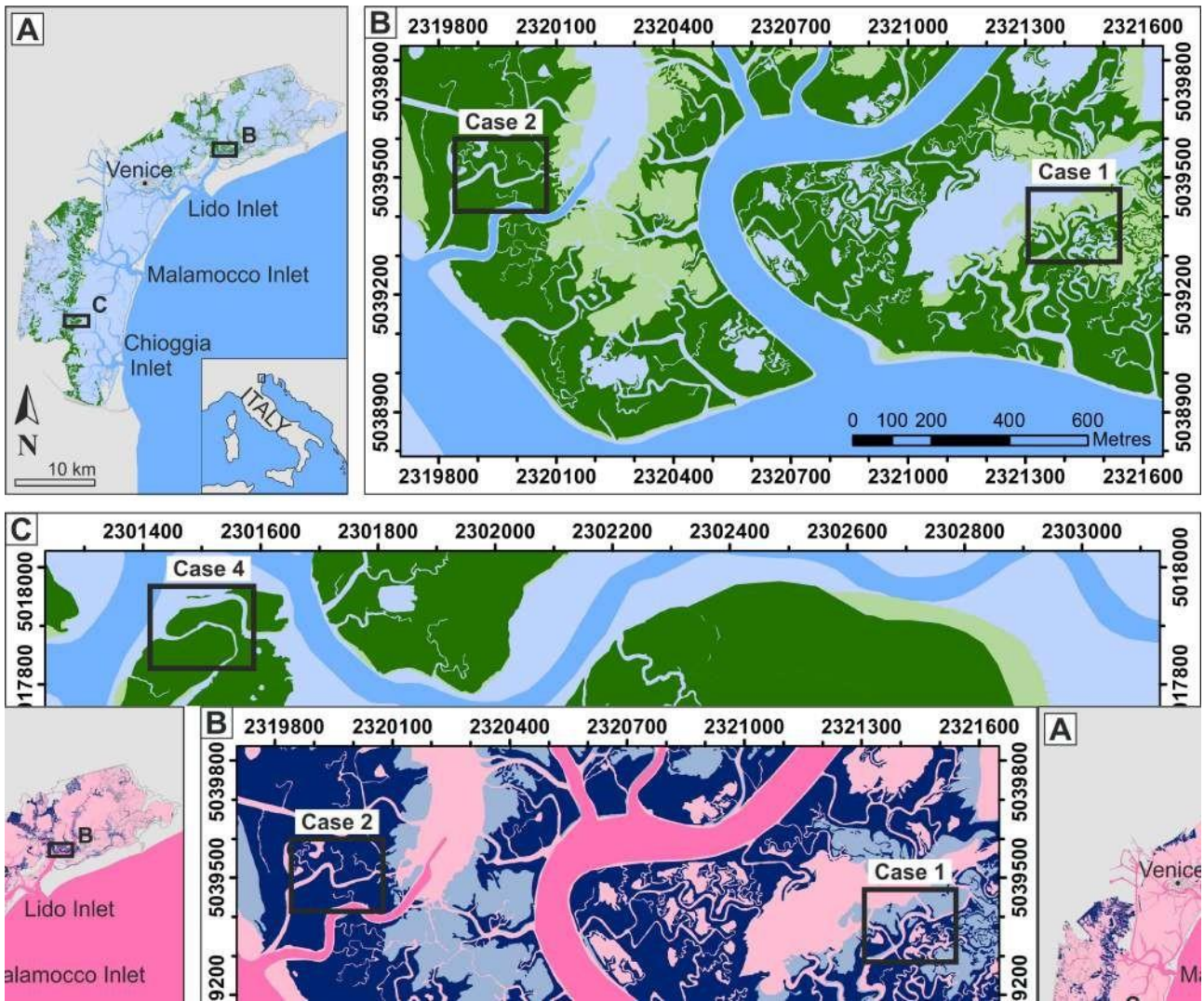


Figure 1

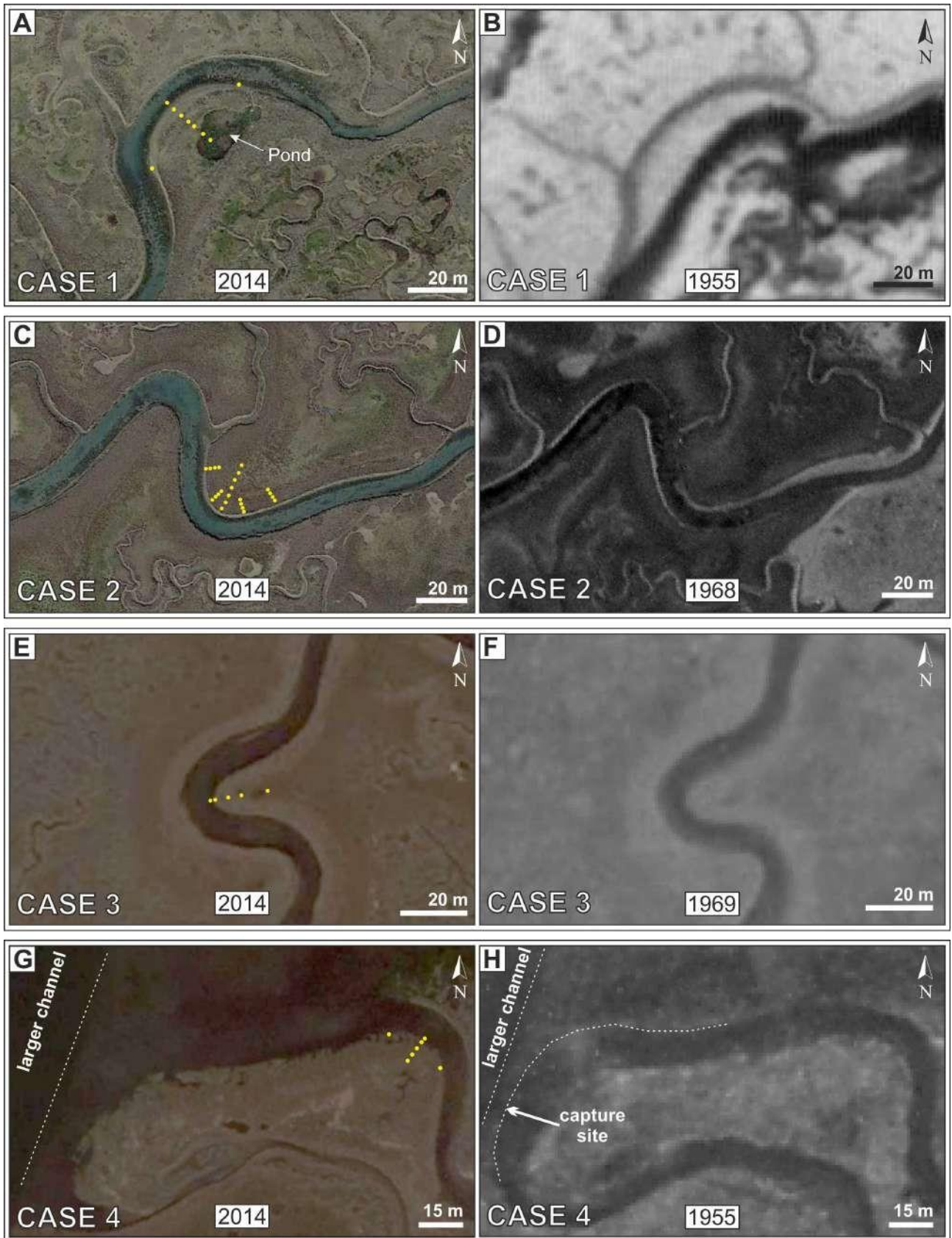


Figure 2

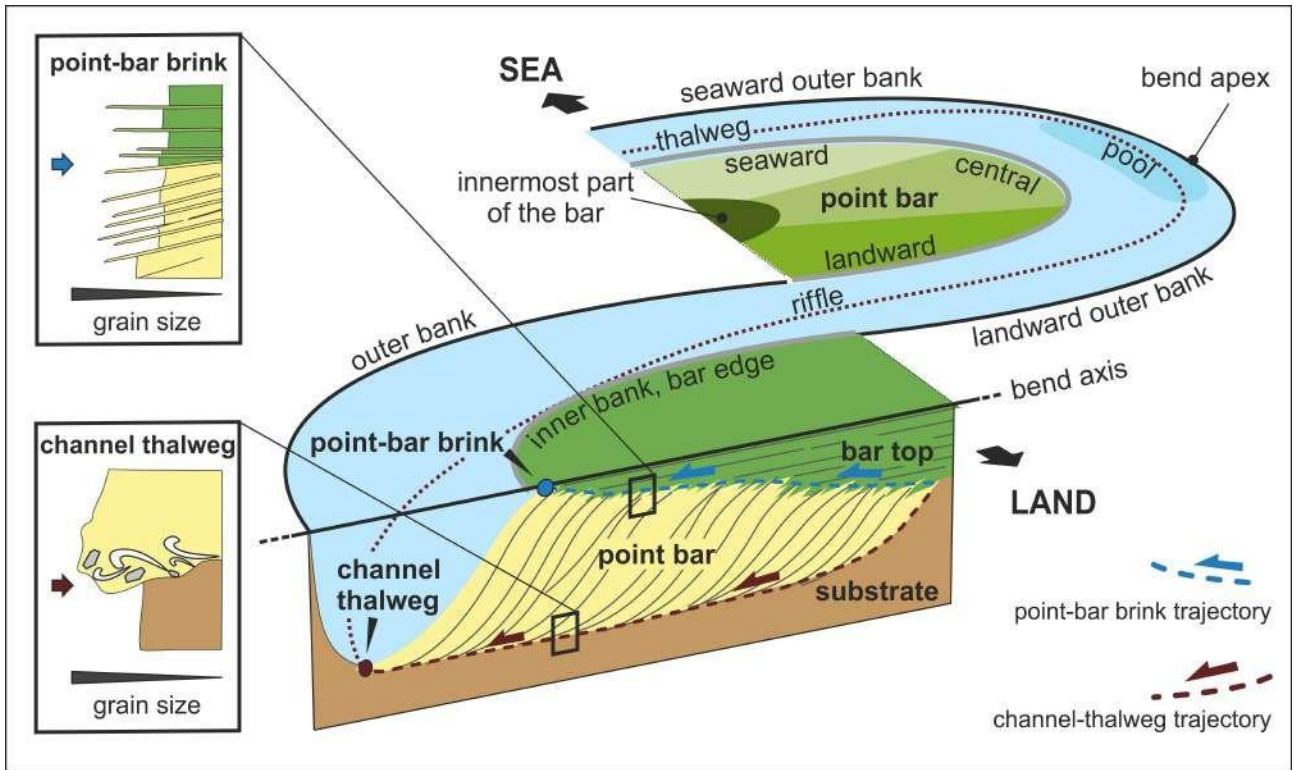
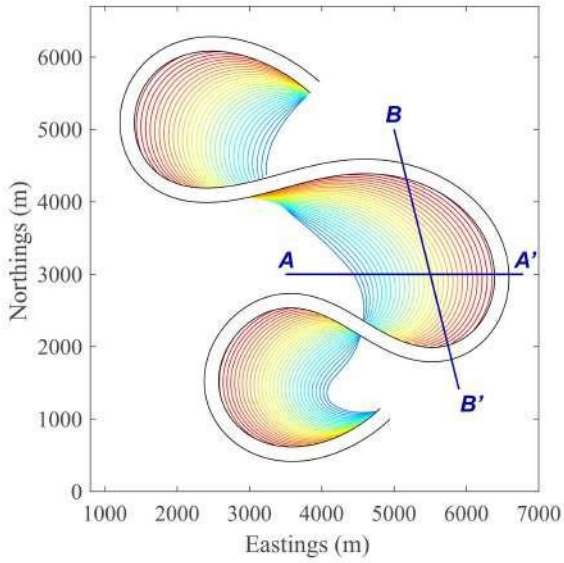


Figure 3

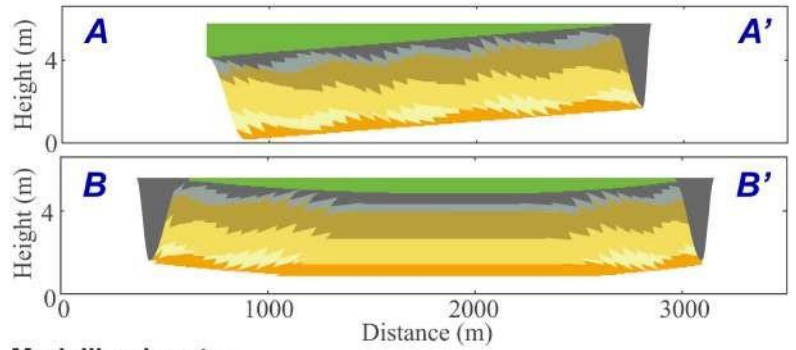
### STEP 1. Planform transformation



#### Modelling inputs:

- point-bar transformation style
- coordinates of channel centreline at two key times at least
- number of scroll bars between key times
- channel width (min-max)

### STEP 2. Cross-sectional geometry



#### Modelling inputs:

- point-bar depth:
  - linear increase (min-max values)
  - list of values for each scroll
- aggradation:
  - linear increase (overall value)
  - list of values for each scroll
- pool-to-riffle bathymetric change (% of max channel depth)

### sedimentary facies

facies associations	shape of bounding surfaces
<ul style="list-style-type: none"> <li>• facies types</li> <li>• proportion of different facies at representative point bar locations</li> </ul>	<ul style="list-style-type: none"> <li>• inclination for each bounding surface</li> <li>• disorder and randomness level for each facies</li> </ul>

Figure 4

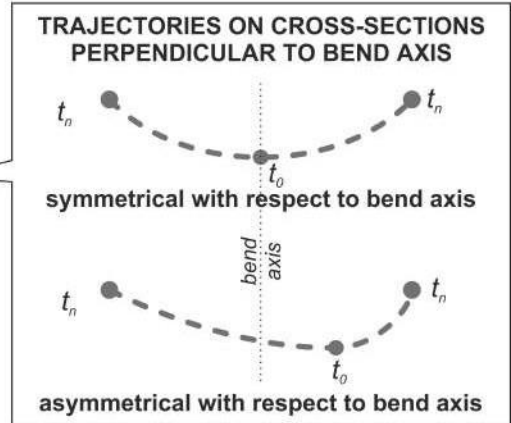
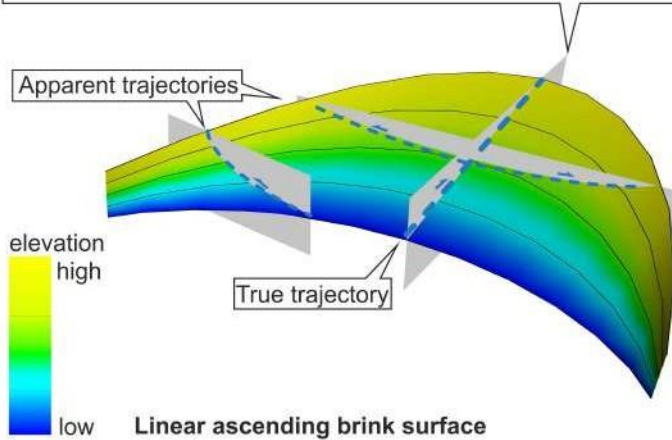
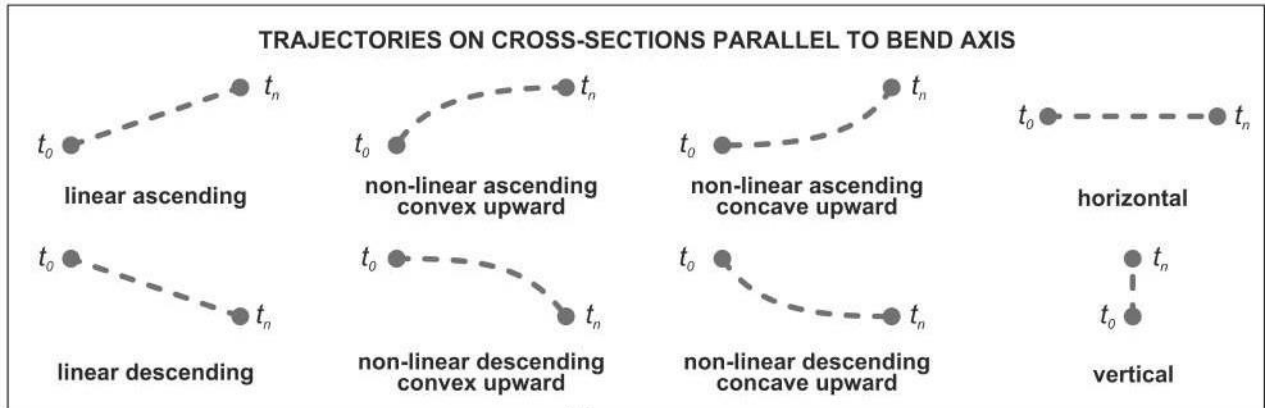
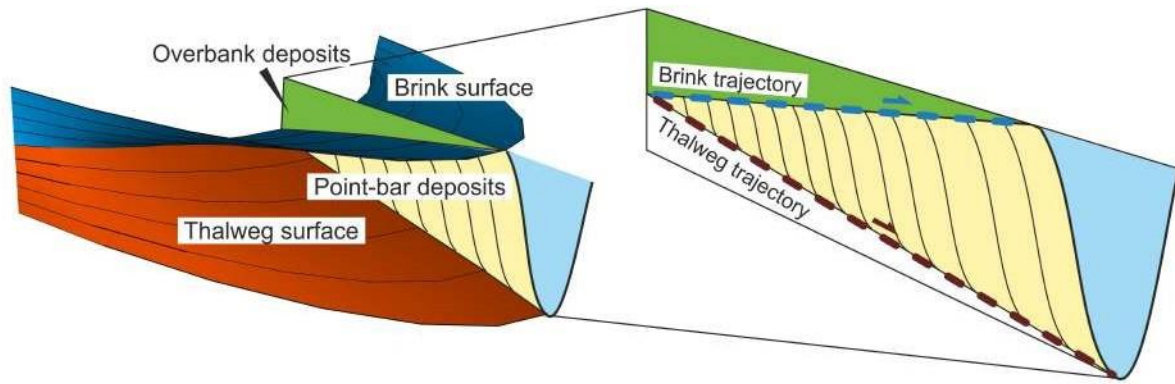


Figure 5



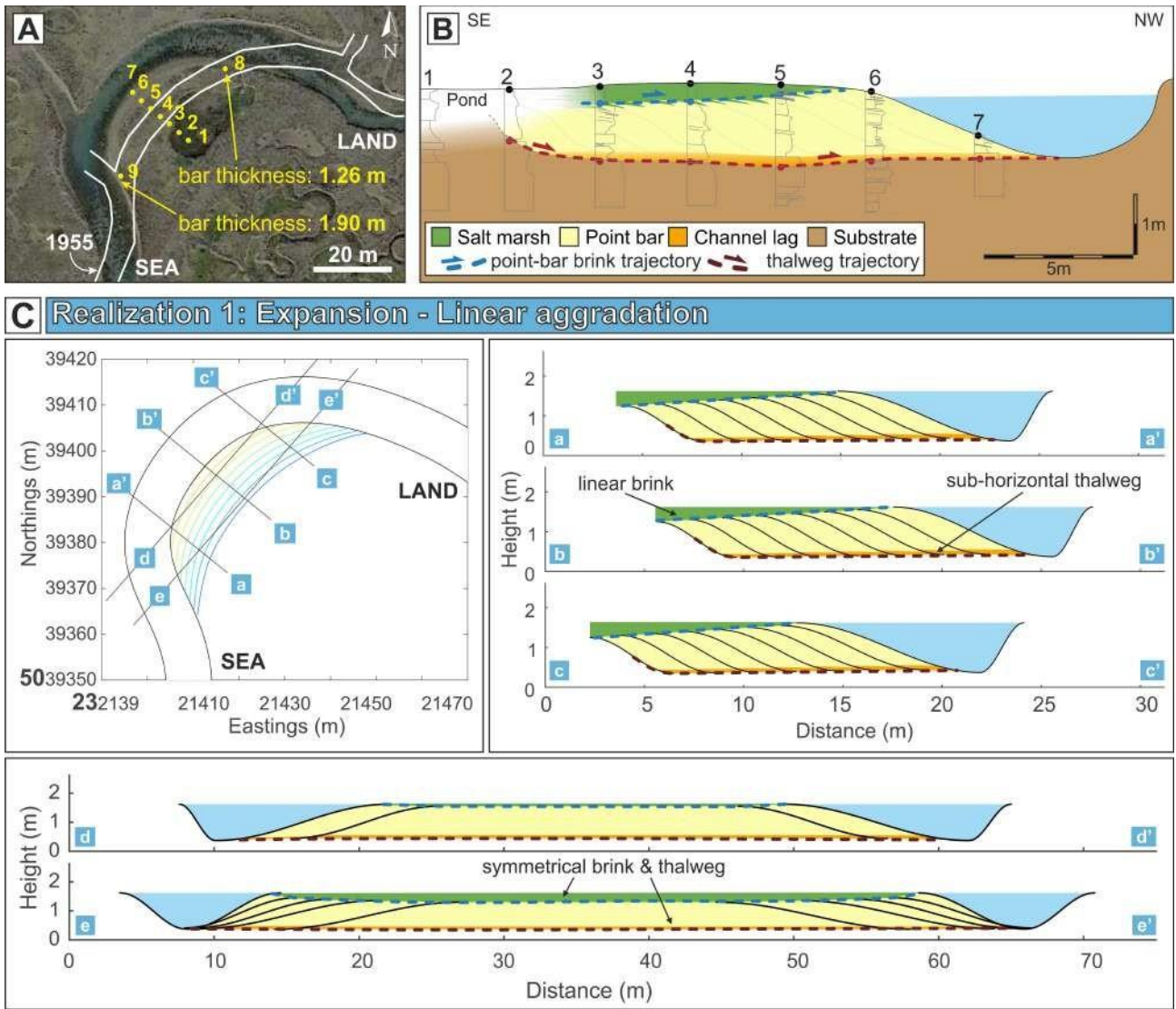
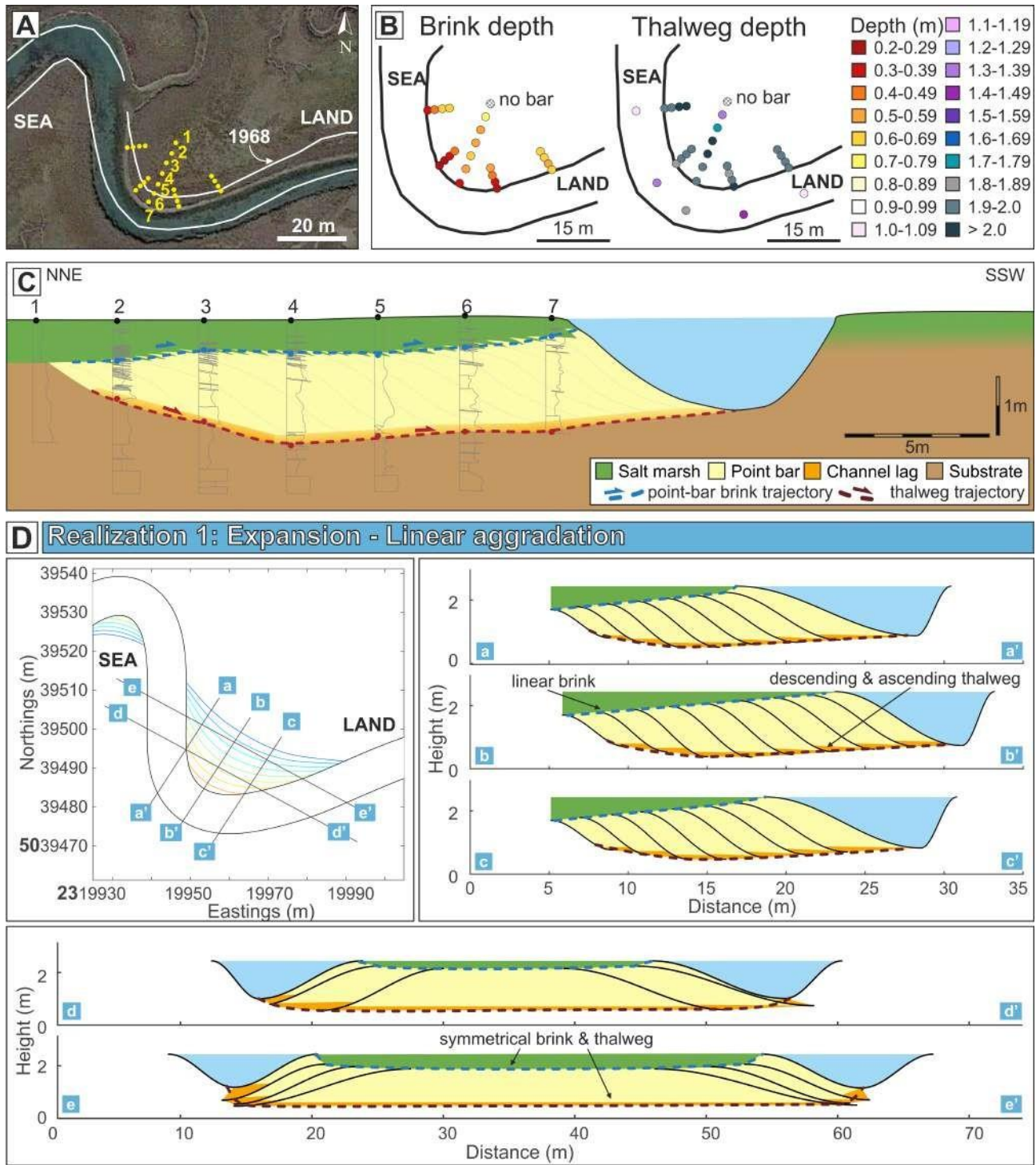
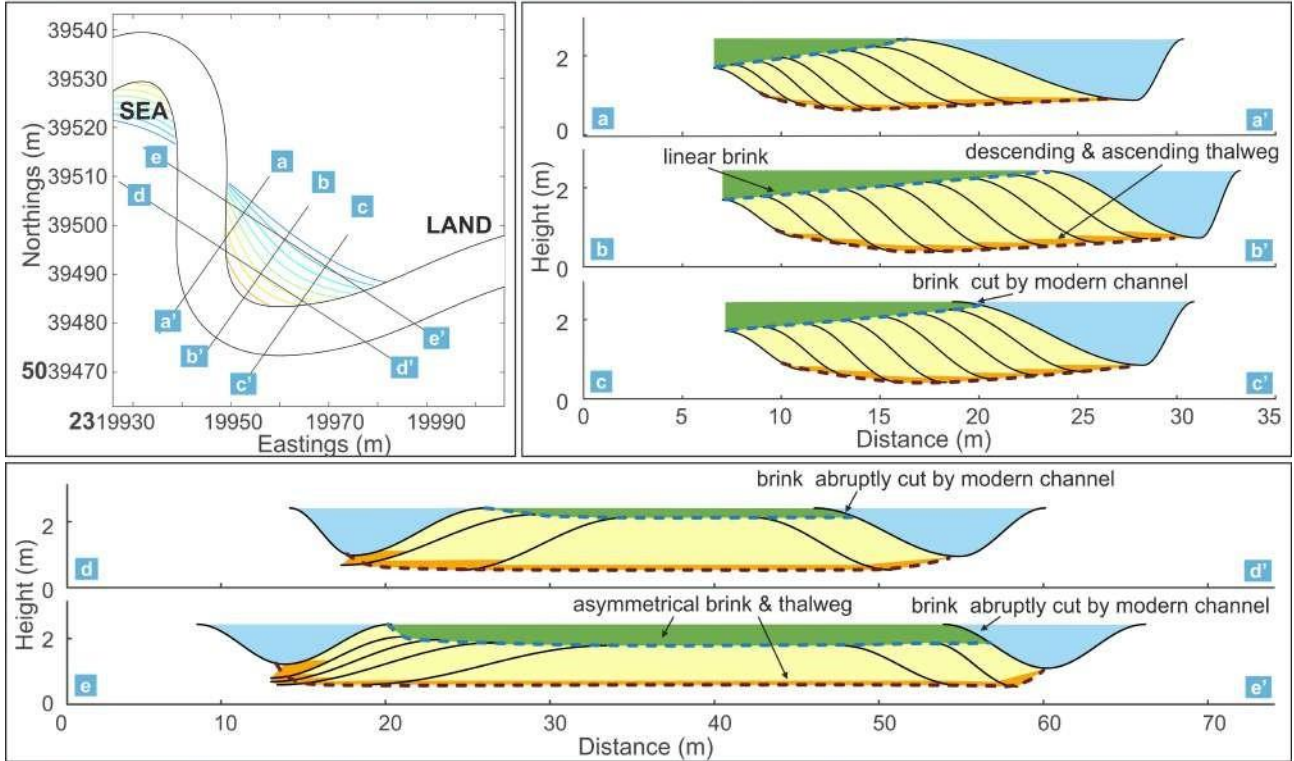


Figure 6



### E Realization 2: Expansion & Rotation - Linear aggradation



### F Realization 3: Expansion & Translation - Linear aggradation

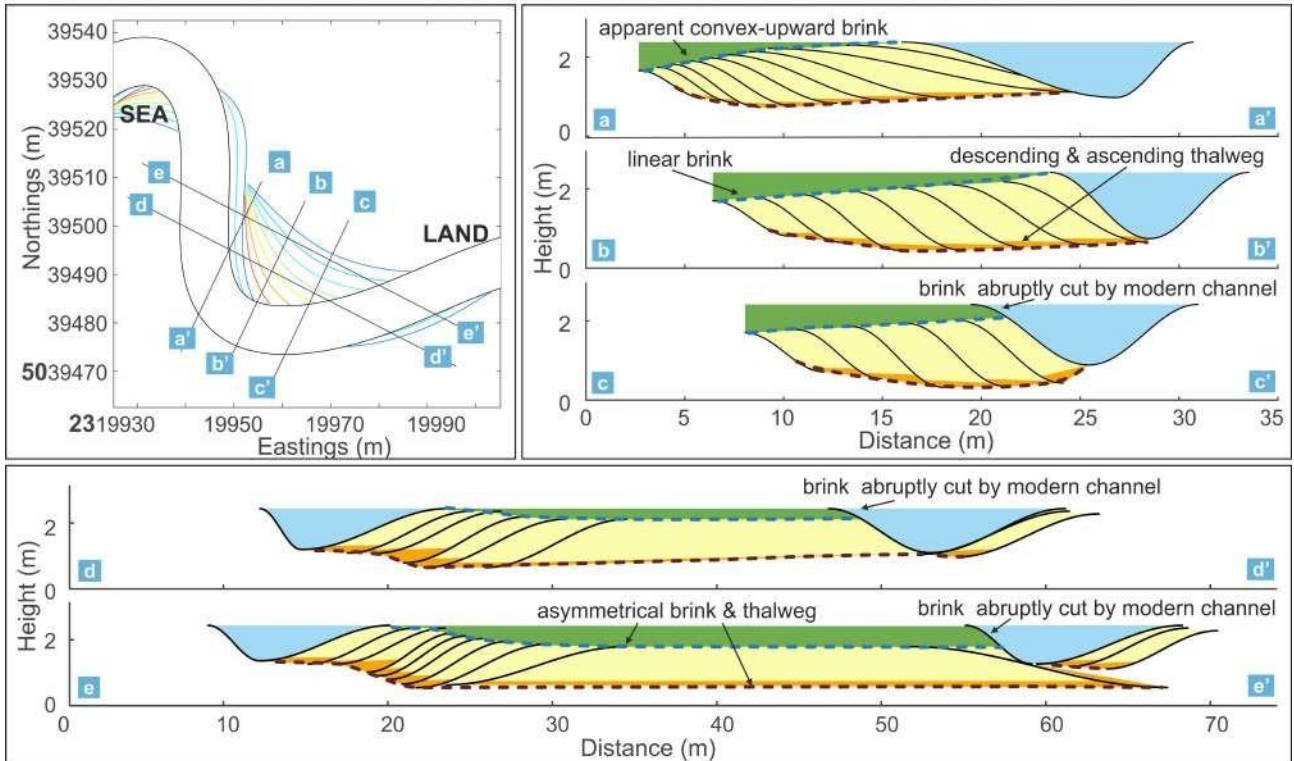
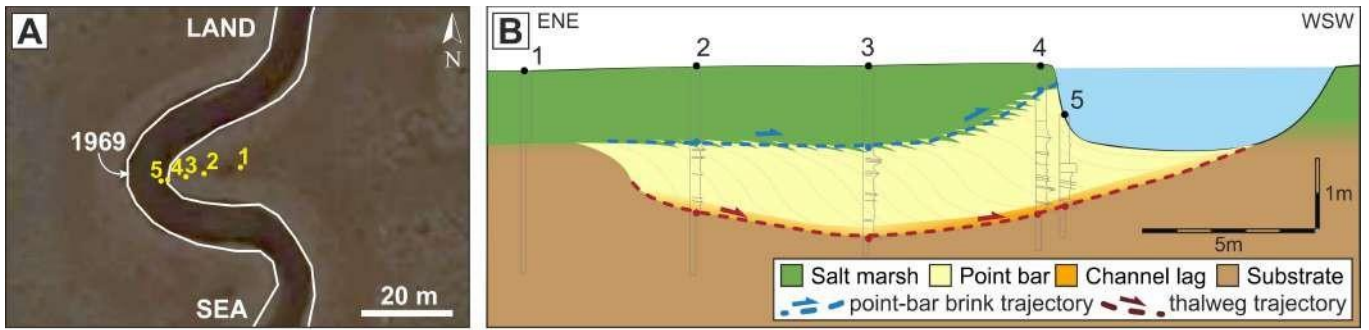


Figure 7 (continued)



**C** Realization 1: Expansion - Non linear aggradation

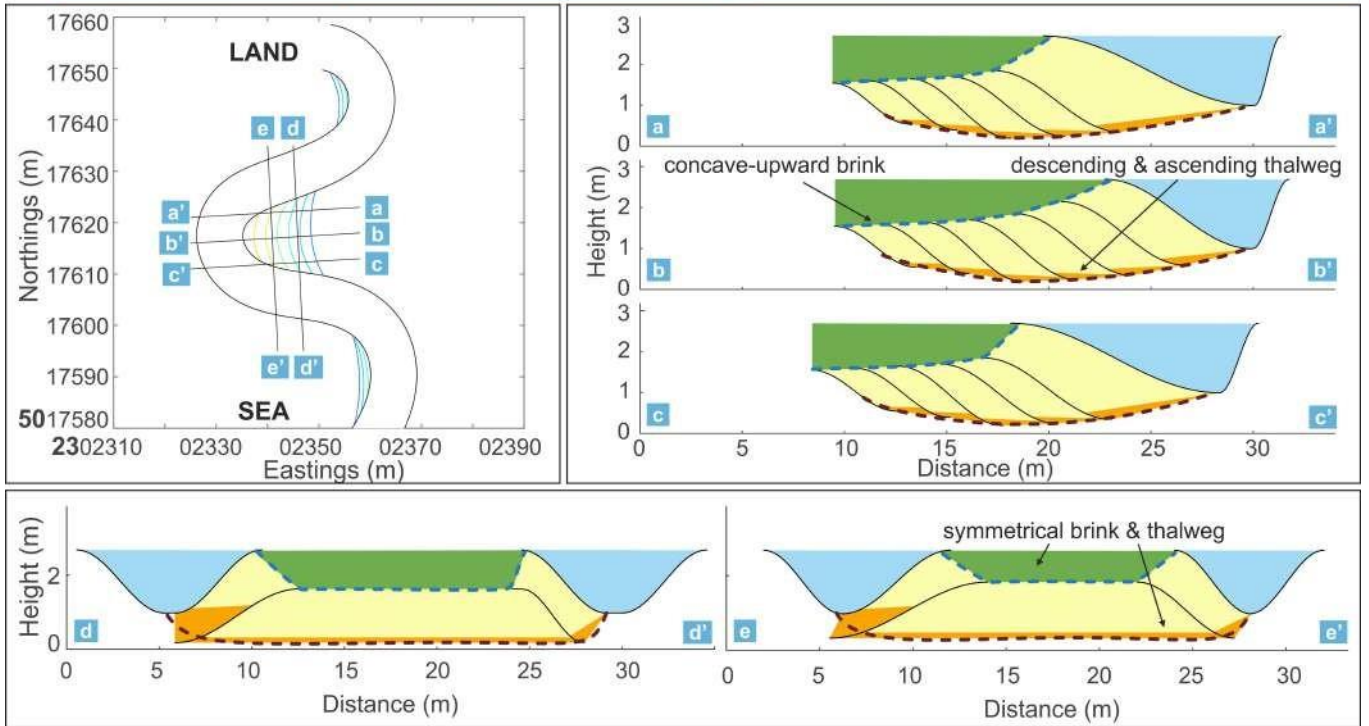


Figure 8 (continuing)

**D** Realization 2: Translation - Linear aggradation

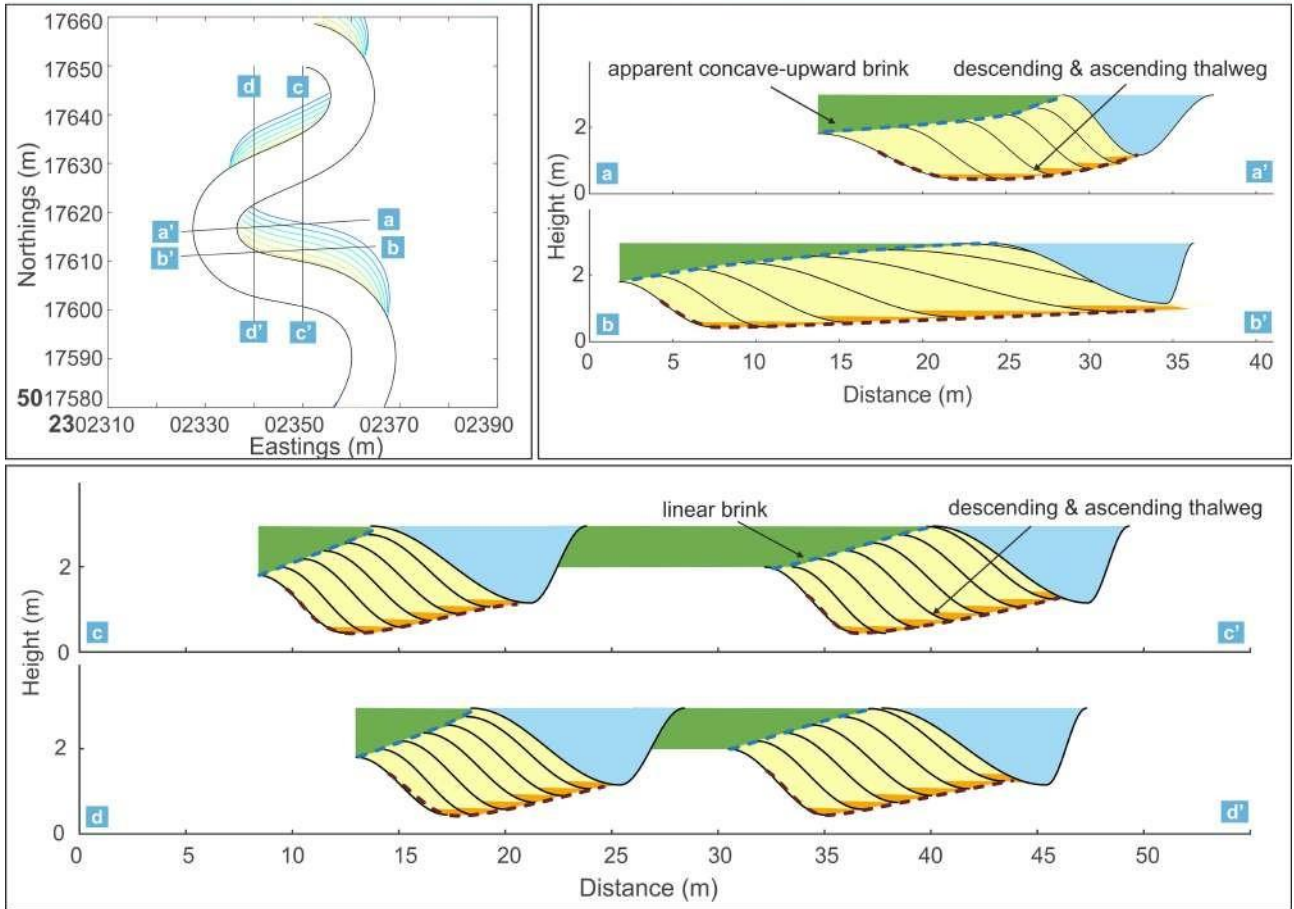
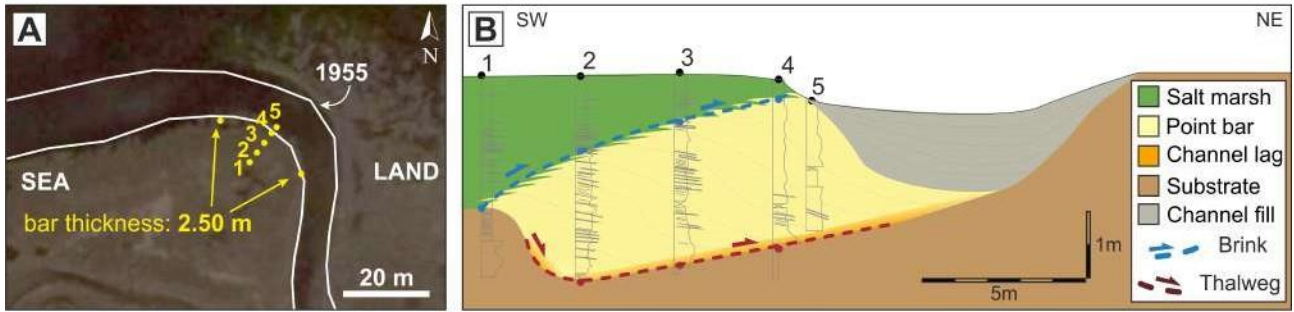


Figure 8 (continued)



**C Realization 1: Expansion - Non linear aggradation**

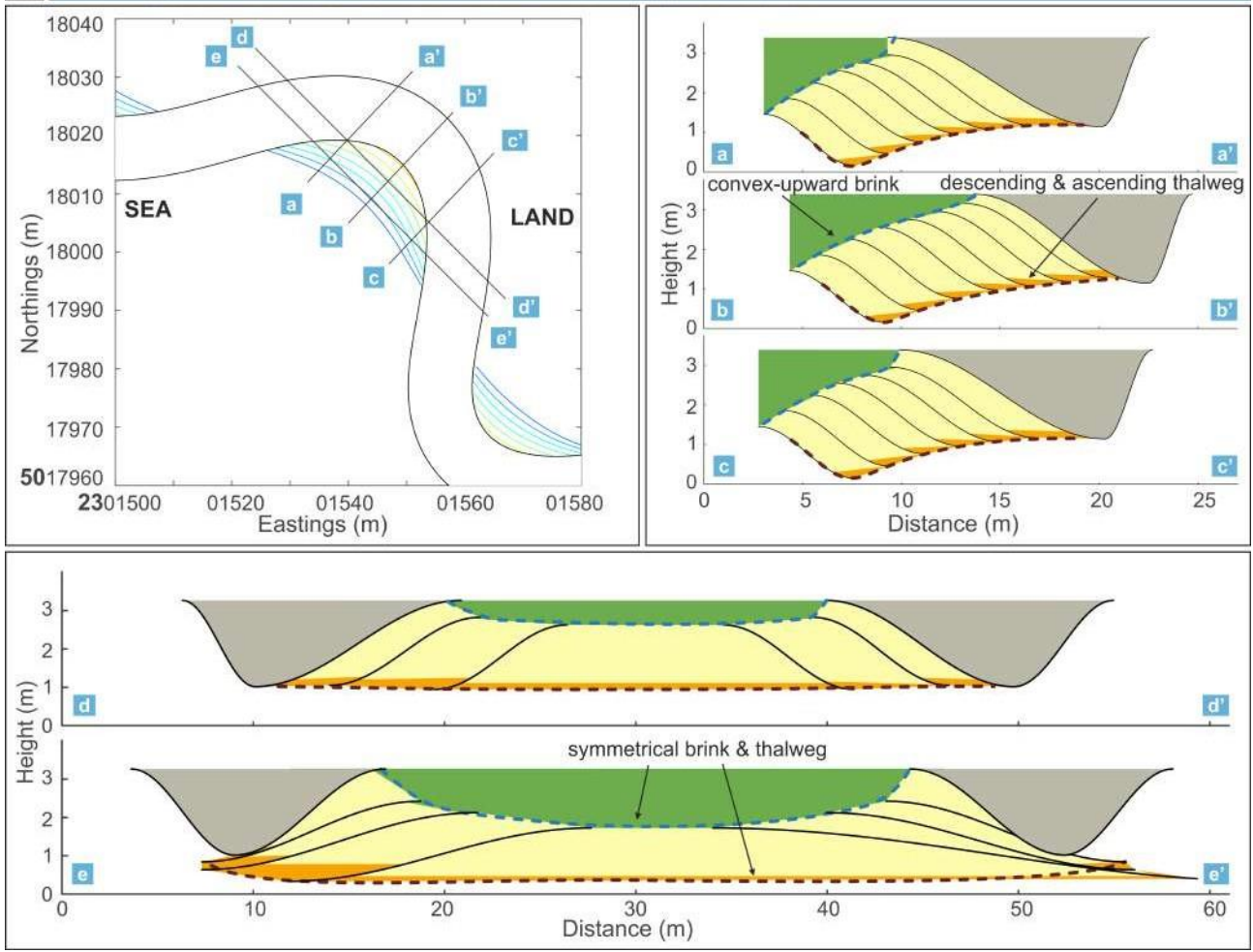
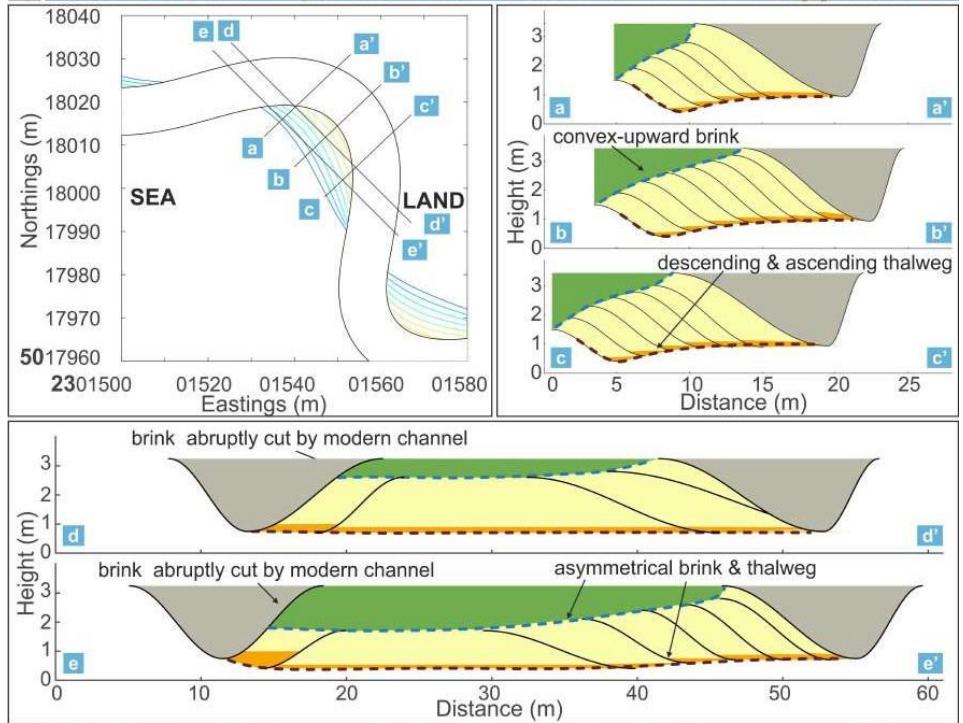


Figure 9 (continuing)

**D Realization 2: Expansion & Rotation - Non linear aggradation**



**E Realization 3: Expansion & Translation - Linear aggradation**

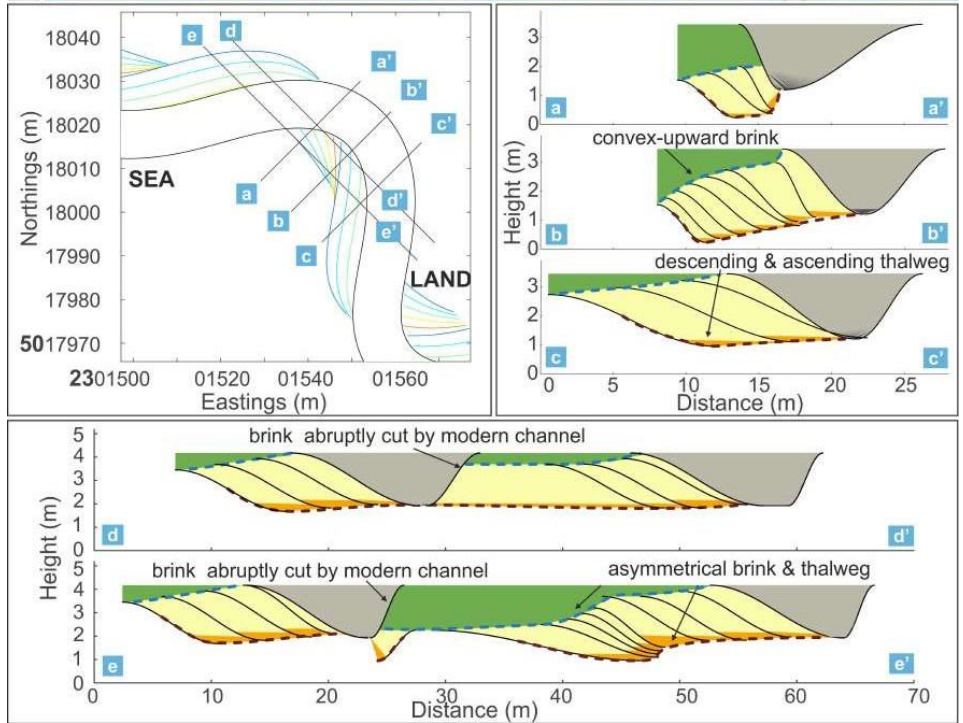


Figure 9 (continued)

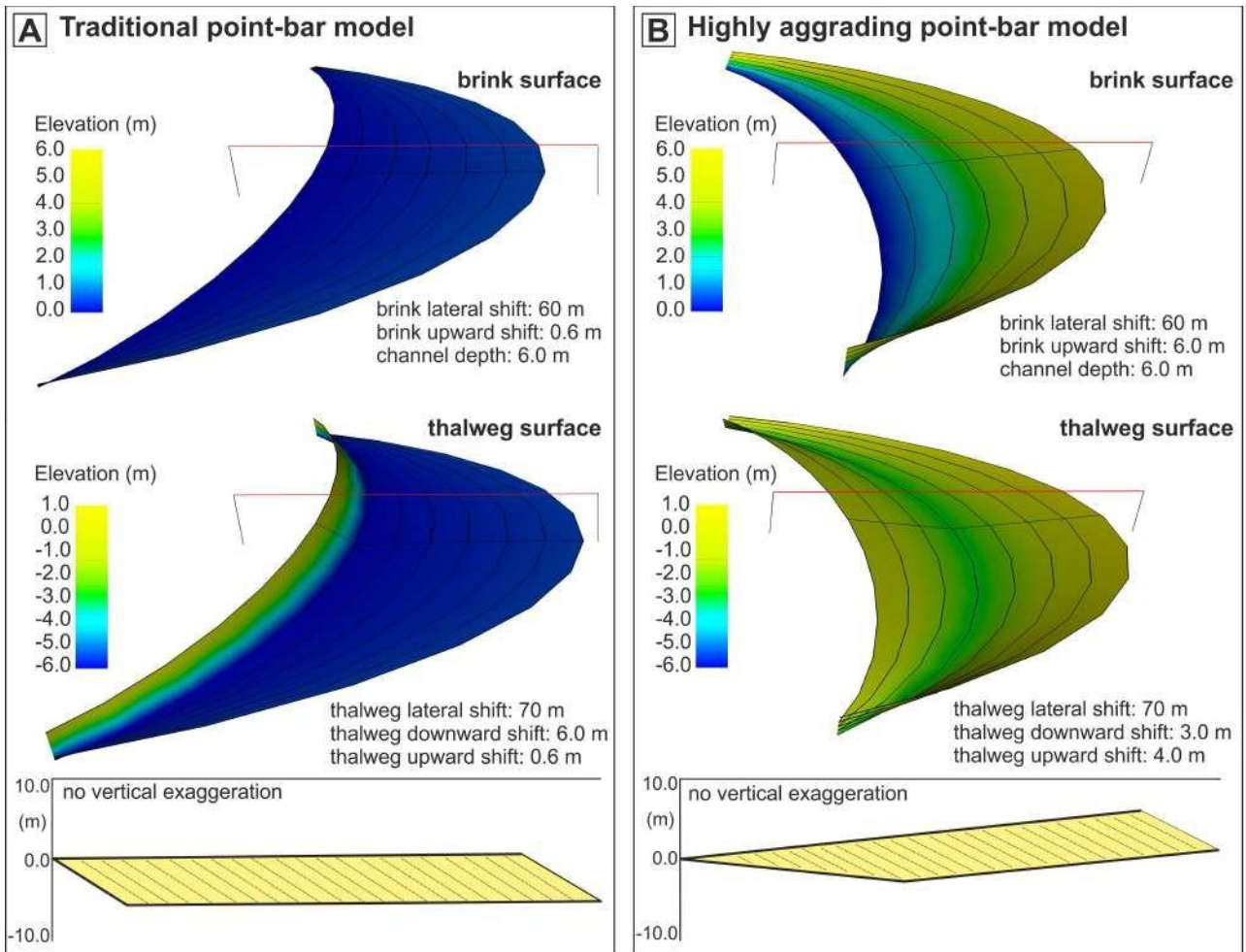
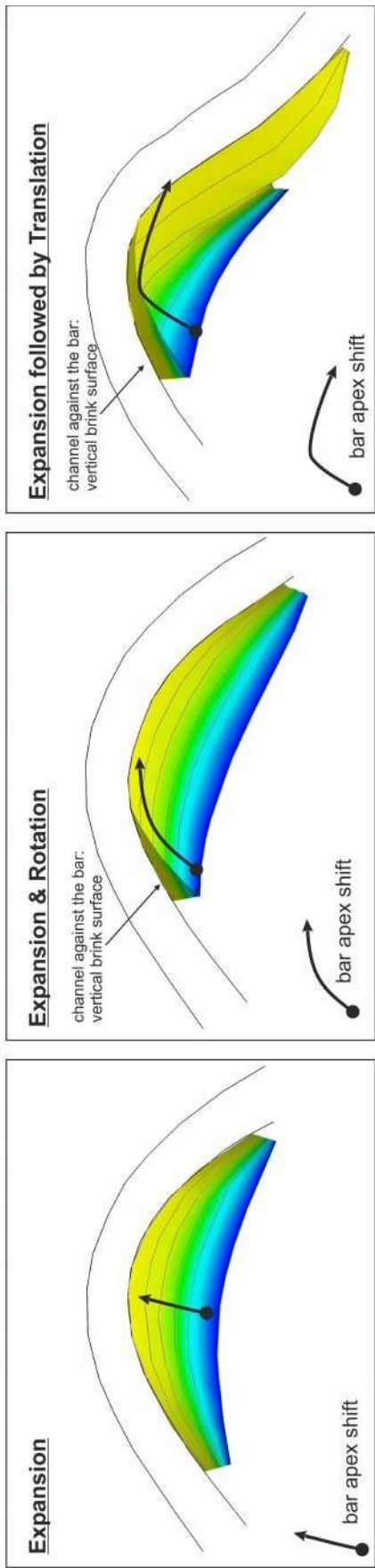


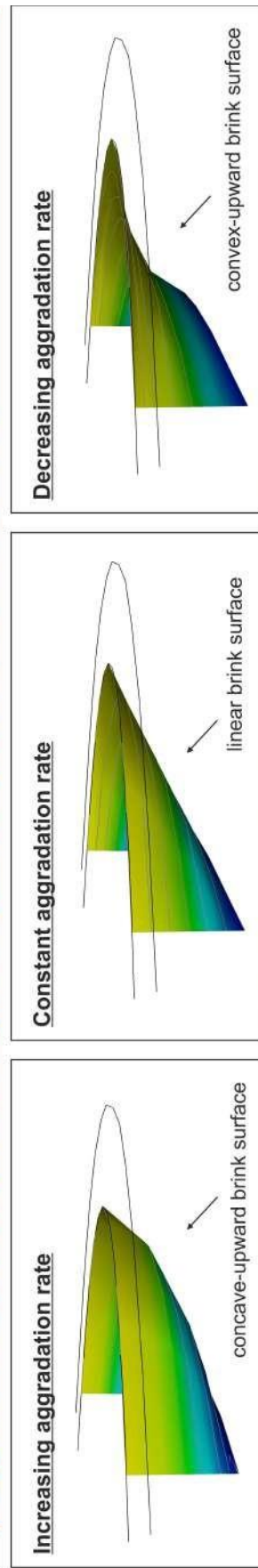
Figure 10



**A** Planform transformation controls point-bar geometry - example on the brink surface



**B** Aggradation controls point-bar geometry - example on the brink surface



**C** Interplay between planform transformation and aggradation - example on the brink surface

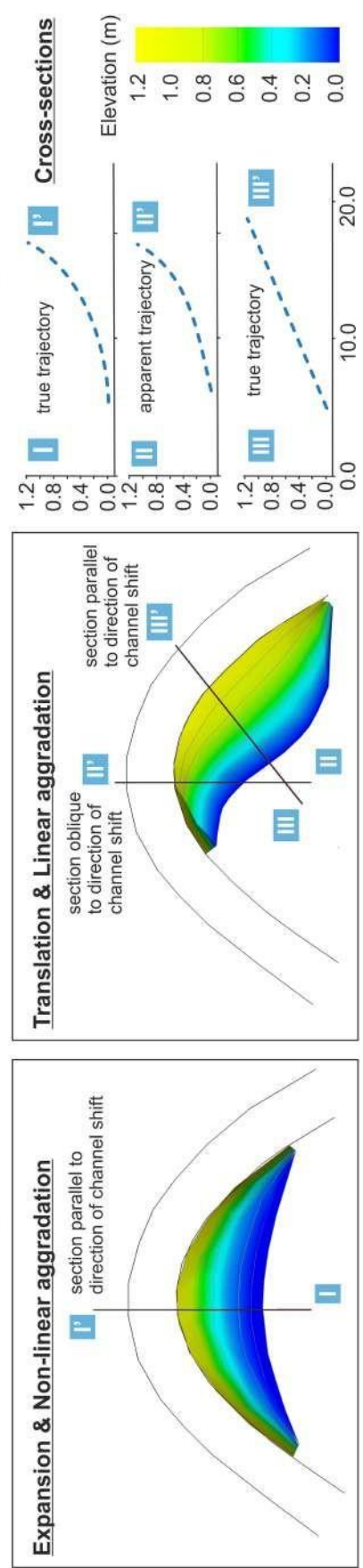


Figure 11

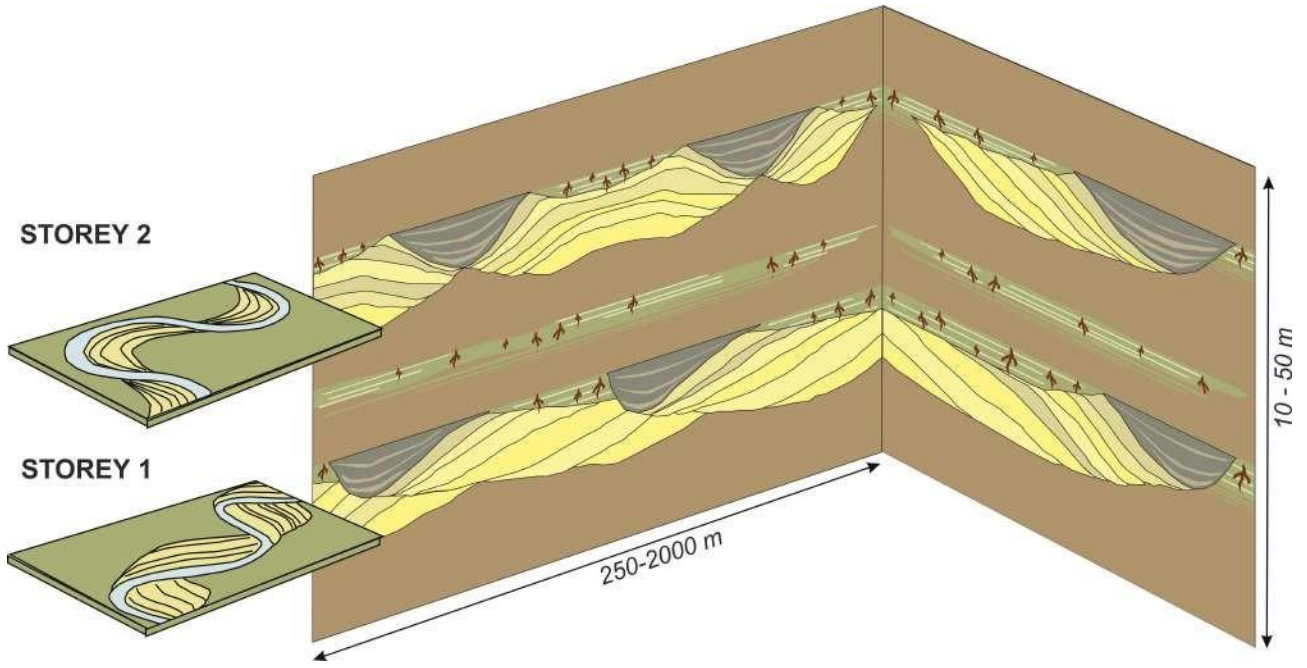


Figure 12